Quantifying the impact of oxidation on the mechanical properties of Alloy 718 using local mechanical testing techniques

Malo Jullien, Marc Legros, Mathieu Calvat, Jean-Charles Stinville, Damien Texier

Materials & Design 259 (2025) 114669

Contents lists available at ScienceDirect

Materials & Design

journal homepage: www.elsevier.com/locate/matdes

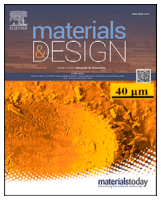

Quantifying the impact of oxidation on the mechanical properties of Alloy 718 using local mechanical testing techniques

Malo Jullien [a,b,*], Marc Legros [b], Mathieu Calvat [c], Jean-Charles Stinville [c], Damien Texier [a,**]

[a] Institut Clement Ader (ICA) - UMR CNRS 5312, Université de Toulouse, CNRS, INSA, UPS, Mines Albi, ISAE-SUPAERO, Campus Jarlard, 81013 Albi Cedex 09, France
[b] Centre d'Elaboration de Matériaux et d'Etudes Structurales, CNRS UPR 8011, 31055 Toulouse cedex 4, France
[c] Materials Science and Engineering, University of Illinois at Urbana-Champaign, USA

ARTICLE INFO

Keywords:
Nickel-based superalloy
Nanoindentation
Micro-pillar compression
Graded-property materials
High resolution-digital image correlation (HR-DIC)

ABSTRACT

Despite excellent oxidative properties of the Alloy 718 Ni-based superalloy, long-term exposure to oxidative environments in service creates a chemical gradient in the sub-surface affected by oxidation. Its characterization is key to assessing the evolving mechanical behavior of such affected materials. The present study focuses on the γ'-γ" precipitation depletion induced by the chemical gradient and benchmarks micro-mechanical testing techniques to assess local mechanical properties. Local techniques such as nanoindentation and micro-pillar compression were used to measure both elastic and plastic properties of a pre-oxidized Alloy 718 Ni-based superalloy, having a chemical gradient. These results were compared to a global approach by tensile testing and high resolution-digital image correlation (HR-DIC) on model materials corresponding to regions of the chemical gradient: the solid-solution and the precipitation-hardened Alloy 718. The plastic behavior was investigated in terms of macroscopic yield strength and slip activity. Results obtained by the local and global techniques were found to be different but complementary. The relevance of the association of multiple micro-mechanical tests and sample preparation techniques to probe chemical gradients is discussed and technique advantages and drawbacks are exposed based on the single crystalline or polycrystalline nature of the micro-mechanical testing.

1. Introduction

Graded microstructures are of great interest whether they are purposely designed for specific applications or result from unwanted processes such as exposure to extreme environments. The improvement of mechanical performances of structural materials may benefit from the growing capability to manufacture controlled heterogeneous microstructures. Few examples of designed heterogeneous microstructures can be found in the literature under the denomination of *functionally graded materials*. These materials are designed – mostly thanks to additive manufacturing techniques – to have a gradient of properties that fit the best their in-service use [1–4]. The nature of these gradients can be either chemical, microstructural (phases, grain size, lamellar thickness, etc.) or both [5]. Among them, dual-alloy components are emerging solutions to benefit from optimized properties at specific locations [6–8]. At the same time, the mechanical properties of existing materials working in harsh environments are often dictated by the sub-surface mechanical gradient induced by the environment. For example, changes in mechanical properties due to local oxidation are critical as they can lead to severe embrittlement and therefore can impede the lifetime of components [9–11]. Similar challenges can be faced with coatings [12], hydrogen absorption [13] or surface plastic deformation [14,15]. Being able to characterize the transitional regions of the gradient and how the different mechanical behaviors interact with each other is central to the design of these materials and their characterization over their lifetime. However, these transitional regions extend over tens of micrometers, making the development of micromechanical characterization a key concern.

* Corresponding author at: Institut Clement Ader (ICA) - UMR CNRS 5312, Université de Toulouse, CNRS, INSA, UPS, Mines Albi, ISAE-SUPAERO, Campus Jarlard, 81013 Albi Cedex 09, France.
** Corresponding author.
E-mail addresses: malo.jullien@mines-albi.fr (M. Jullien), damien.texier@mines-albi.fr (D. Texier).

https://doi.org/10.1016/j.matdes.2025.114669
Received 1 May 2025; Received in revised form 28 July 2025; Accepted 28 August 2025

Available online 9 September 2025

In the present study, a combined experimental framework was applied to address the effect of the micrometer-scale precipitation depletion due to high temperature oxidation on the mechanical response of the Alloy 718 Ni-based superalloy. This alloy is widely used for industrial applications at intermediate temperature (below 650 °C) in oxidative environments such as aeronautical and terrestrial turbines or primary circuit of nuclear power plants. Its microstructure can vary depending on the application but it is mostly used in its precipitation-hardened metallurgical state. In this case, the Alloy 718 is hardened by $\gamma'' - (Ni_3Nb)$ and $\gamma' - (Ni_3(Ti, Al))$ precipitates. When exposed to temperature higher than 650 °C, $\delta - (Ni_3Nb)$ phase can precipitate from the $\gamma'' - (Ni_3Nb)$ phase, thus decreasing the fraction of $\gamma'' - (Ni_3Nb)$ and its associated strengthening. According to thermodynamic calculations [16] supported by experimental observations [17], when exposed to high temperatures, the Alloy 718 develops internal Al_2O_3 oxides at grain boundaries and a protective external Cr_20_3 layer. Depending on the oxidation kinetics, titanium- and niobium-rich oxides can also form. Oxidation is a selective phenomenon leading to the diffusion of alloying elements such as Al, Cr, Nb or Ti towards the surface and/or the grain boundaries. This diffusion process can be accompanied by the formation of a precipitation-depleted zone in the sub-surface affected by oxidation [9]. Since the mechanical properties of precipitation-hardened materials are closely related to their precipitation state [18,19], understanding the mechanical behavior of the oxidation-affected region is of great interest to better predict the mechanical integrity of structural components exposed to oxidative atmospheres.

As it has been widely discussed in the literature, at room temperature, Alloy 718 deforms by the formation, multiplication and intensification of slip bands [20–24]. In the case of a γ'' precipitation-hardened Alloy 718, slip bands are mainly located at the interior of grains and the most intense events are parallel and close to annealed twin boundaries [20,21,23,25,26,24]. This strain localization, also denoted parallel slip configuration, was reported as a preferred initiation site of fracture during a fatigue test at room temperature [20,26].

The understanding of the mechanical behavior of a graded sample involves a local characterization of the transitional regions at the scale of the gradient. These characterizations can be obtained from surface observations using optical or electron microscopy (identification of carbides, pores, size of particles, size of grains, crystallization, etc.) [27] or in the volume (porosity, phases, carbides, etc.) [28], chemical (phases density and size, segregation, light elements (C,H,O,N, etc.) diffusion, etc.) [29,30] or mechanical (strong elastic differences, heterogeneities, weak features, dislocation sealing, etc.) [31–33]. Emerging capabilities for the high-throughput micro-mechanical testing has made possible to locally probe mechanical properties of materials [34–36]. Conventional nanoindentation and high speed nanoindentation mapping (HSNM) at the microstructure scale are promising techniques to reveal local variations of mechanical properties with relatively low effort in specimen preparation [37–41,31,42]. However, the inverse identification of mechanical properties (directional Young's modulus, yield strength, strain hardening, etc.) is complex due to the multi-axial loading conditions under the indentation tip and the mechanically probed volume increasing with the indentation depth. To greatly simplify the loading conditions, micro-pillar compression tests offer the advantages of a much more uniaxial loading for property identification and intermediate skills for FIB machining. However, size effects could significantly affect the mechanical response due to surface effects, *i.e.*, free surface versus machining-affected surface, the probed volume and the occurrence of dislocation sources, etc. [43,44]. Micro-tensile testing, which requires much more FIB preparation, can also inform on the role of tensile-compression anisotropy response when compared to micro-pillar compression testing [45]. All these techniques, generally performed for "monocrystalline" cases, present the advantage of assessing force vs. displacement curves at the microscale to quantitatively dissociate the mechanical behavior of materials at the microstructure scale.

High resolution-digital image correlation (HR-DIC) techniques [46–55] or topographic measurements [21,56–58] are very efficient means to quantify strain localization in polycrystalline materials at different scales. While these techniques are used for fine and local assessment of deformation at the microscale, they do not provide local stress fields, essential for a full identification of the mechanical response. However, they enable the investigation of neighborhood effects due to surrounding grains on the deformation response of a given grain embedded in a crystalline aggregate. One challenge with HR-DIC is the need for a nanoscale speckle pattern to capture strain localization. All these micromechanical techniques present advantages and drawbacks to capture the strain localization and mechanical behavior of materials at the scale of the microstructure. They are all pertinent and complementary for the investigation of the elementary deformation mechanisms. However, the application of all these techniques to document strain localization in terms of intensity and spatial distribution has not yet been investigated.

In the present work, the effect of the metallurgical state, *i.e.*, the solid-solution form or the precipitation-hardened form, of the Alloy 718 has been investigated in terms of local mechanical response, strain heterogeneity and strain localization at the sub-grain level using different micromechanical methods. The change in metallurgical state due to high temperature oxidation was addressed using a combination of nanoindentation and micro-pillar compression tests to identify mechanical properties over the oxidation-affected region and differences in slip activity. The slip activity characteristics were compared with HR-DIC measurements performed on bulk samples to characterize the role of a polycrystalline aggregate on the strain localization capability of the Alloy 718. It was studied in both its solid-solution form (first microns in the oxidation-affected region) and its precipitation-hardened form (bulk specimen).

2. Material and methods

2.1. Material

The material considered in the present study is a polycrystalline Ni-based superalloy, the Alloy 718. Its nominal composition is the following: Bal. Ni, 18.57 % Cr, 18 % Fe, 5.02 % Nb, 2.86 % Mo, 0.11 % Co, 0.58 % Al, 0.97 % Ti, <0.01 % Ta (weight percent). Three different metallurgical states were investigated to document the effect of the precipitation state on the overall mechanical response and strain localization capability of the materials. These properties were evaluated using either nanoindentation, micro-pillar compression or tensile testing paired with HR-DIC. Both nanoindentation mapping and micro-pillar compression tests were performed on a precipitation-hardened sample with a chemical gradient near the surface due to high temperature oxidation conditions (samples #1 and #2). For the HR-DIC measurements, bulk samples were used in a precipitation-hardened form (sample #3) and solid-solution form (sample #4) to represent the bulk material and oxidation-affected region, respectively. All the samples were extracted from a 635 μm-thick rolled sheet of the same nominal composition for further reproducibility of the experiments.

2.2. Sample preparation for the different micromechanical tests

2.2.1. Preparation of the oxidation-affected samples

Two samples with a chemical gradient due to high temperature oxidation were prepared, one for nanoindentation (sample #1) and another with coarser grains for micro-pillar compression (sample #2). Coupons extracted from a 635 μm-thick rolled Alloy 718 sheet were first polished up to P4000 SiC grit paper. The specimens were heat-treated under air at 1180 °C (above the γ', γ'' and δ solvus temperature) for 5 and 25 hours, for nanoindentation (sample #1) and micro-pillar compression (sample #2), respectively. This step aims at both introducing a chemical gradient using the oxidation properties of Alloy 718 and increasing the

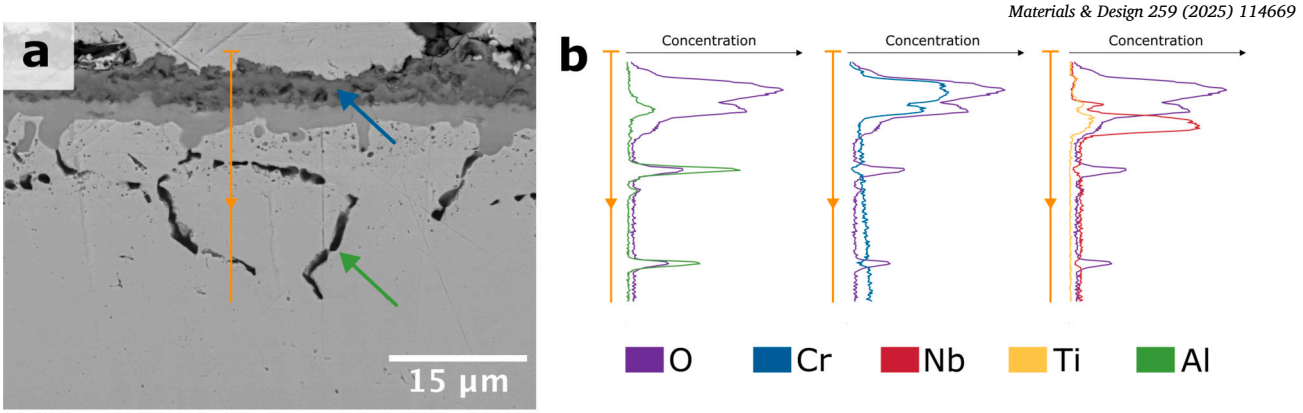

Fig. 1. (a) Microstructure of the oxidation-affected region of the Alloy 718 sample #1 (backscattered electron imaging modality on the specimen cross-section). Blue and green arrows points at the chromia (Cr_2O_3) external oxide scale and alumina (Al_2O_3) internal oxides, respectively. (b) EDS profile analysis along the orange line plotted in the SEM micrograph.

grain size. Both samples #1 and #2 were then subjected to a two-step heat-treatment under vacuum to introduce the gradient of precipitation in the oxidation-affected material: a first dwell at 720 °C for 8 h, followed by a cooling at 50°C.h^{-1}, and a second dwell at 620 °C for 8 h, followed by a slow furnace cooling.

As aforementioned, the oxidation-affected region is characterized by a chemical gradient due to the selective nature of the high-temperature oxidation. Cross-sectional specimens were cut with a precision cutting machine and then mounted in cold epoxy with low shrinkage properties to protect the adhesion of the external oxide scale. The samples were then polished using conventional metallographic methods to 1/4 µm with diamond suspensions and then finished with 0.05 µm colloidal silica suspension. The microstructures of the oxidized samples were observed in backscattered electron mode using a SEM Nova NanoSEM 450 (Thermo Fisher Scientific, NLD) equipped with an Apollo X SDD detector (EDAX, USA) and analyzed with TEAMS^{TM} (EDAX, USA). The microstructure of the oxidation-affected region of sample #1 is depicted in Fig. 1(a). The oxidation-affected region consists of (1) an external chromium-rich oxide layer (chromia: Cr_2O_3, dark gray pointed by the blue arrow in Fig. 1(a)), (2) a complex niobium/titanium-rich oxide layer beneath the Cr_2O_3 layer (intermediate gray in Fig. 1(a)) and (3) internal oxidation of alumina (Al_2O_3) at grain boundaries (black pointed by the green arrow in Fig. 1(a)). As further detailed, the Alloy 718 is deprived of precipitation beneath the external oxide scale and a precipitation gradient is formed towards the specimen core. EDS profiles were performed in the oxidation-affected region to quantify chromium depletion (Fig. 1(b)). The chromium content is minimal beneath the outer oxide layer and increases slightly toward the core of the sample. These observations are in good agreement with the ones reported in the literature [16,17].

The oxidation-affected region of sample #1 extends over tens of micrometers in depth, as shown in Fig. 1(a) and about 3 times deeper in sample #2 due to a longer exposure to air at 1180 °C. In order to better probe the mechanical properties of the resulting chemical gradient, samples #1 and #2 were purposely prepared using precise wedge-cut techniques to spread the gradient of chemical composition over several hundreds of microns, as in Ref. [59]. To do so, the wedge-cut samples were prepared by mechanical polishing using a precision jig and a spacer for high-tolerance specimen machining [60]. This process is illustrated in Fig. 2 top right corner. A spacer of known thickness is placed under the sample at one end and glued to a rectified glass slide using thermal wax. Then, the inclined sample is mechanically polished on SiC papers (up to P4000 grit papers) using a custom precision jig device which allows a high precision and good flatness of the sample [60,9]. The sample was then manually polished down to 1 µm with diamond suspensions, followed by vibropolishing with 0.05 µm colloidal silica suspension for 2 hours. A SEM micrograph in backscattered electron mode of the resulting wedge-cut sample is shown in Fig. 2. Taking the internal oxidation depth as a reference and comparing with the cross-section SEM image (Fig. 1), the gradient of microstructure has been spread over hundreds of microns (350 µm for the wedge-cut sample compared to 20 µm for the cross-section sample #1). An EDS mapping was carried out on the wedge-cut sample to validate the spread of the chemical gradient (Fig. 2). Indeed, it can be seen on the EDS overlay that the niobium-rich oxide layer which is about 2 µm thick (see Fig. 1) spreads over tens of micrometers. This also allows to identify an additional thin titanium-rich layer (TiO_2) under the niobium-rich layer. This specific sample preparation is essential for further nanoindentation and micro-pillar compression tests.

2.2.2. *Preparation of the solid-solution and precipitation-hardened tensile specimens for HR-DIC*

Flat dogbone-shape specimens were extracted from the Alloy 718 sheet. Two metallurgical states were considered: (1) the precipitation-hardened state corresponding to the bulk material (sample #3) and (2) the solid-solution state corresponding to the material in the oxidation-affected region beneath the external oxide scale (sample #4). Both samples #3 and #4 were heat-treated at 1050 °C for 30 min and air-quenched to obtain the solid-solution state (sample #3). For the precipitation-hardened state (samples #4), the two-stage heat treatment was additionally applied (720 °C-8 h then 620 °C-8 h). The flat dogbone-shape specimens were then manually polished on all faces to remove the region affected by machining and the heat treatments. The flat surfaces of the specimens were polished to 1 µm with diamond suspensions followed by vibropolishing with 0.05 µm colloidal silica suspensions for 2 hours.

2.2.3. *Other characterization means*

Additional metallurgical characterizations were conducted using transmission electron microscopy (TEM) on a JEOL 2010 HC microscope to document the precipitation state within the oxidation-affected material. STEM-EDX analyses were performed on a CM20 FEG-TEM (JEOL, JPN) equipped with a EDX SDD detector (Bruker, USA) and on the Esprit 1.9 software.

Several EBSD devices were used depending on the samples. EBSD mapping measurements performed on sample #1 (for nanoindentation purposes) were carried out on a MEB FEG JEOL JSM-7100F TTLS LV (JEOL, JPN) equipped with EBSD CMOS Symmetry S2 detector with a step size of 0.5 µm (Oxford Instruments, GBR). For sample #2, local EBSD measurements were performed before micro-pillar FIB-milling on a Helios NanoLab 600i FIB-SEM (Thermo Fisher Scientific, NLD) equipped with an EBSD CMOS detector with a step size of 0.2 µm (Oxford Instruments,

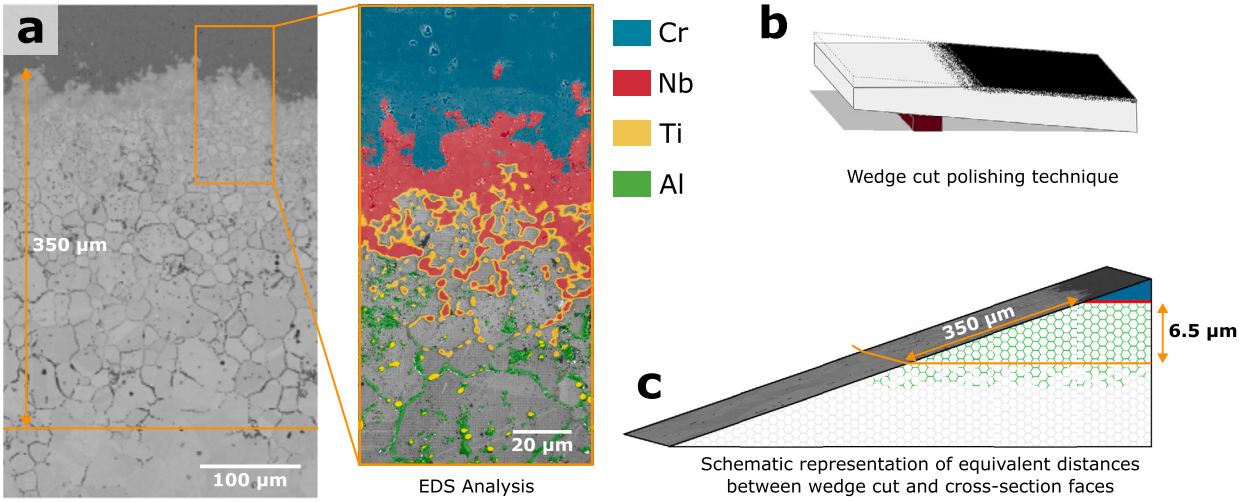

Fig. 2. Representation of the wedge-cut sample #1. (a) SEM micrograph of the wedge-cut sample surface in backscattered electron mode. EDS element maps are overlaid on the magnified region showing the different locations of the oxide layers. (b) Schematic illustration of the wedge polishing technique. (c) Schematic distances comparison of the wedge-cut sample with the cross-section, where the color code is the same as for EDS mapping.

GBR). Finally, EBSD measurements were obtained on samples #3 and #4 before deformation using an EDAX OIM-Hikari XM4 EBSD detector with a step size of 0.7 µm. Diffraction patterns were acquired using an accelerating voltage of 20 kV, a 2×2 binning and a beam current of 0.2 nA.

2.3. Mechanical testing

2.3.1. High speed nanoindentation mapping (HSNM) and conventional nanoindentation (CN)

Both micromechanical tests – high speed nanoindentation mapping (HSNM) and conventional nanoindentation (CN) – were performed using a NMT-04 system (Femtotools, CHE). HSNM characterizations were performed *ex-situ* on sample #1 on the surface obtained by the wedge-cut preparation technique. Tests were displacement driven at a loading rate of $3.10^{-2}\ \mu m.s^{-1}$ using a diamond Berkovich tip and a 20 mN load cell. The continuous stiffness measurement (CSM) method was used, allowing to evaluate the reduced modulus and the hardness values as a function of depth. Both the reduced modulus and hardness values stabilized beyond a critical penetration depth, ensuring that the measurements are representative of local properties in the volume. For HSNM, a 125 nm penetration depth was used and indents are spaced 1.5 µm apart. In total, 7,250 indents were performed to cover the region of interest. The hardness and reduced modulus values were calculated as the average of the respective properties during the loading phase from 70 to 120 nm contact depth.

Conventional nanoindentation was also performed on the same system with the same Berkovich tip and load cell. Tests were also displacement driven but the CSM method was not employed. A lower loading rate of $1.10^{-3}\ \mu m.s^{-1}$ was used to detect stress drop on the indentation curves when they occur. The chemical gradient in sample #1 was characterized by multiple lines of 150 nm-deep indents using a 20 µm spacing. A total of 915 indents were analyzed across the chemical gradient. The stress drops contained in the local stress-displacement curves were identified and their amplitude was measured thanks to a Python routine based on the Scipy library.

2.3.2. Micro-pillar compression testing

The micro-pillar compression tests were performed *in-situ* in the Helios Nanolab 600i SEM-FIB (Thermo Fisher Scientific, NLD) using a NMT-04 system (Femtotools, CHE). The micro-pillars were first FIB-milled in the same microscope on sample #2 using an annular milling strategy. Micro-pillars have a square cross-section of 3 × 3 µm and a height of about 10 µm, respecting a 1/3 ratio between the side length and height of the pillars. For each grain studied, a line of three pillars was milled at iso-chemical composition for repeatability. For the compression tests, a 10 µm-diameter flat punch and a 200 mN load-sensor were used. During the tests, SEM images were continuously recorded in order to correlate the slip activity arising at the pillar surface to events in the stress-strain curves (stress drop, strain deviation, etc.). For the compression tests, the experimental data were post-treated following a two-step process. A first step aimed to extract "Stress-Strain" curves from the raw Force/Displacement curves. To do so, the force is divided by the cross-section of the pillar and the displacement is divided by the height of the pillar. The second step of the post-treatment process is the detection and extraction of stress drops in the plastic regime. Each event was detected using the same Python routine used for conventional nanoindentation.

2.3.3. High resolution-digital image correlation (HR-DIC)

First, samples #3 and #4 were machined by electrical discharge machining (EDM) in a dogbone tensile specimen shape with a gage section of 3 mm × 1 mm. The specimens were then mechanically polished with SiC papers up to 1200 grit, followed by diamond suspension to 3 µm and a chemo-mechanical polishing with 50 nm colloidal silica for 12 hours. To produce the speckles, layers of 10 nm of titanium and 3 nm of silver were deposited on the sample surface using an AJA ATC 2200-V Sputter Coater (AJA international, USA). The upper silver layer was reconfigured into particles by immersing the samples in a 1 % salt water solution at room temperature for 2 hours. Further details of the procedure can be found in Ref. [61,62].

High-resolution imaging was then performed on a Versa3D field emission gun system SEM/FIB (Thermo Fisher Scientific, NLD) for high resolution-digital image correlation (HR-DIC). The imaged area consists of a grid of 8 by 8 secondary electron images collected with 15 % overlap between adjacent images and resulting in a 1.2 mm by 1.2 mm area. The 4096×4096 pixel images were acquired with a field of view of 138 µm, an accelerating voltage of 10 kV, a current of 0.9 nA, a dwell time of 20 µs per pixel, and a working distance of 5 mm. SEM parameters were selected according to the guidelines from Ref. [48,49,63]. The images were taken before deformation, and mechanical testing was then interrupted at increasing levels of macroscopic plastic strain to take new images of the deformed region. Based on the strain calculated by HR-DIC, the precipitation-hardened Alloy 718 specimen (sample #4) was interrupted at 0.17 %, 0.32 %, 0.61 %, and 1.26 % of macroscopic plastic strain and the solid-solution Alloy 718 specimen (sample #3) was interrupted at 0.24 %, 0.48 %, 0.88 %, and 1.81 % of macroscopic plas-

tic strain.

The in-plane slip amplitude was estimated using the Heaviside-DIC (H-DIC) technique [23]. More details can be found in Ref. [64]. All HR-DIC calculations were performed using a proprietary software (XCorrel, FRA) and were computed with respect to the undeformed state. A subset size of 31×31 pixels and a step size of 3 pixels were used for the calculations. Data from the HR-DIC experiments are available through DRYAD [65,66].

3. Results

3.1. Characterization of the oxidation-affected region

As mentioned before in the "material and methods" section, the microstructure of the oxidation-affected region was characterized using SEM imaging and EDS analyses (Fig. 1). To better correlate the chemical state to the mechanical properties, the oxidation-affected region was characterized both chemically and mechanically. The SEM-EDS analyses shown in Fig. 2(b) were supplemented by STEM-EDX analyses. A FIB-prepared TEM sample was extracted from the sample #1 at the location indicated in Fig. 3, *i.e.*, at the end of the internal oxidation of Al_2O_3 at grain boundaries. On the TEM dark-field micrograph shown in Fig. 3(a), the sample surface is located in the upper part of the micrograph. Near the end of the internal oxidation of Al_2O_3, the material is depleted of precipitates. However, δ and γ'' precipitates are found at approximately 2 to 3 μm below the lamella surface and their amount increases with the depth. Fig. 3(b) shows a TEM bright-field micrograph of the transitional area marked by the orange rectangle in Fig. 3(a). STEM-EDX analyses evidenced niobium-rich phases confirming the cohabitation of both δ and γ'' precipitates. The small disk-shaped particles and the coarser needle-shaped particles were attributed to the γ'' (Ni_3Nb) and δ (Ni_3Nb) precipitation, respectively. Small oxide particles (tens of nanometers) are also present in this oxidation-affected region. The bright particle in Fig. 3(b) is a titanium-rich oxide. According to these results, it is possible to delineate three areas within the gradient of chemical composition:

- A precipitation-free zone (PFZ) which can be assimilated to a solid-solution Alloy 718. On the wedge-cut surface, the PFZ corresponds to the area where internal oxides are formed at the grain boundaries.
- A transitional region where both γ'' and δ precipitates can be found in small amount, especially for the δ-phase precipitation which is sparsely distributed in this area. This region can be identified at the surface of the wedge-cut sample, where only a few grain boundaries are oxidized.
- A γ'' precipitation-dense area which can be assimilated to a precipitation-strengthened Alloy 718. This area is located below the transitional area, where no oxide was observed at grain boundaries.

The chemical description of the gradient was supplemented by a mechanical characterization presented in Fig. 4. This characterization was performed using the HSNM technique to assess both the reduced modulus *Er* and hardness *H* properties at the sub-grain level. The area tested is centered on the transitional area. As it can be seen on the SEM micrograph in Fig. 4(a), internal oxide can be found at grain boundaries in the upper part, indicating the precipitation-free region. In the lower part of the SEM micrograph, no oxidation is observed at grain boundaries, corresponding to the precipitation-dense region. In between, only a few grain boundaries are oxidized which is typical of the transitional region. The regularly spaced indents of the HSNM map are also visible on the micrographs. Magnified views from the SEM micrograph of both the precipitation-free (orange box) and the precipitation-dense (blue box) regions are shown in Fig. 4(a). The size of the indents are equal in both regions due to displacement control, indicating that the elastic volume probed along the chemical gradient remains consistent.

The reduced modulus map did not evidenced significant elastic evolution between the precipitation-free and the precipitation-dense area (Fig. 4(c)). The reduced modulus is dependent on the grain orientation with the $< 001 >$ direction being the softest direction in the Alloy 718, in agreement with Ref. [42]. Based on the small region of interest, the contribution of the grain orientation and the precipitation on the reduced modulus map cannot be dissociated. A larger testing region using high-throughput nanoindentation and inverse identification method is needed to determine whether the γ'' precipitation has an influence on the elastic anisotropy of Alloy 718 or not.

The precipitation was found to have a significant effect on the hardness response (Fig. 4). The precipitation-dense region exhibits much higher hardness values than the precipitation-free region. Values in bold font on the colorbar legend are the average values of the two magnified views from the SEM micrograph. Within the precipitation-dense region, the average hardness is 6214 MPa, while the average hardness within the precipitation-free region is 5276 MPa. In the transitional region, the hardness is between the average values found at both ends, showing the gradual hardness increase from the oxidation-affected region to the specimen core.

3.2. Probing plastic response through nanoindentation

Conventional nanoindentation tests carried out across the gradient of sample #1 demonstrated stress-drop like behavior. Nanoindentation pop-ins, *i.e.*, a long stress plateau, are commonly observed on the stress-displacement curves as a plastic response from the material when tests are force driven. The first pop-in is associated with the initiation of plasticity. For the following events, the origin of this plastic activity is very sensitive to the microstructure, whether it is due to slip bands formation, particle shearing, interactions of dislocations with grain boundaries, etc. [67]. The present tests are displacement driven, meaning that instead of displacement bursts (pop-ins), stress drops are observed as a plastic response. An example of a stress-drop is shown on the stress-displacement curve in Fig. 5(a). The green curve corresponds to the raw stress-displacement extracted from the nanoindentation test which presents a stress-drop on the magnified view. Several of them are observed for each indentation curve but their number and amplitude vary. In order to identify trends in the plastic activity of both the precipitation-free and precipitation-dense regions of the gradient, a statistical analysis was carried out. For each of the 915 indents, the stress-drops were identified on the loading indentation curve (Fig. 5(a)) and their amplitude was measured as shown on the magnification of Fig. 5(a). Although possible, the unloading part of the indentation curves was not used to measure the hardness or the reduced modulus as we focused here on the onset of plasticity. Then, the sum of stress-drop amplitude for each indent was compared with other indents. The stress-drop amplitude sums are plotted in Fig. 5(b), with each point corresponding to an indentation test. Indents are divided in 3 categories with a specific color-code according to their position in the microstructure:

- Indents closer than 1.5 μm from a grain boundary or an oxide particle. This 1.5 μm limit corresponds to the theoretical radius of the elastic volume probed by a 0.15 μm-deep indent.
- Indents located between 1.5 μm and 5 μm away from a grain boundary or an oxide particle.
- Indents located at least 5 μm away from a grain boundary or an oxide particle.

This segmentation aims at isolating the effect of precipitation from the role of grain boundaries and oxide particles. However, results exposed in Fig. 5(b) show that this segmentation has no impact on the average amount of stress-drop amplitude regardless of the metallurgical state (precipitation-hardened or solid-solution). This suggests that the nanoindentation set-up and the parameters used do not highlight any influence of the grain and twin boundaries on the local stress-

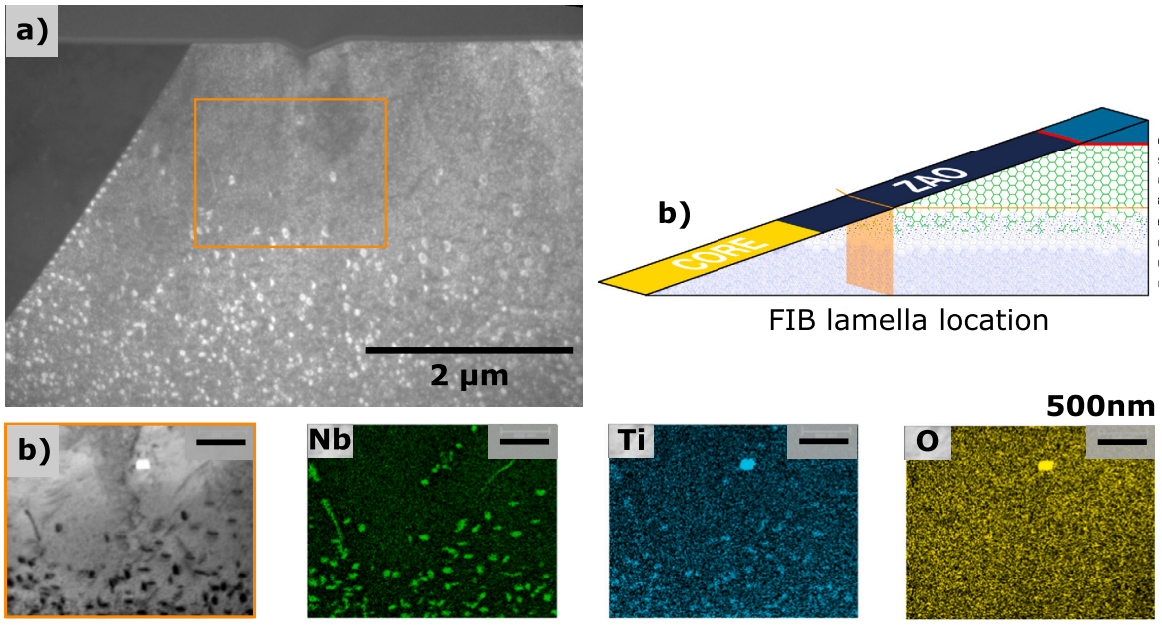

Fig. 3. STEM-EDX analysis. (a) TEM dark field micrograph of the TEM sample showing the gradient of precipitates. (b) Schematic illustration of the position of the TEM sample in the chemical in the zone affected by oxidation (ZAO). (c) TEM bright field micrograph of the orange rectangle insert and corresponding STEM-EDX analysis showing niobium-rich precipitation related to the γ'' and δ phases.

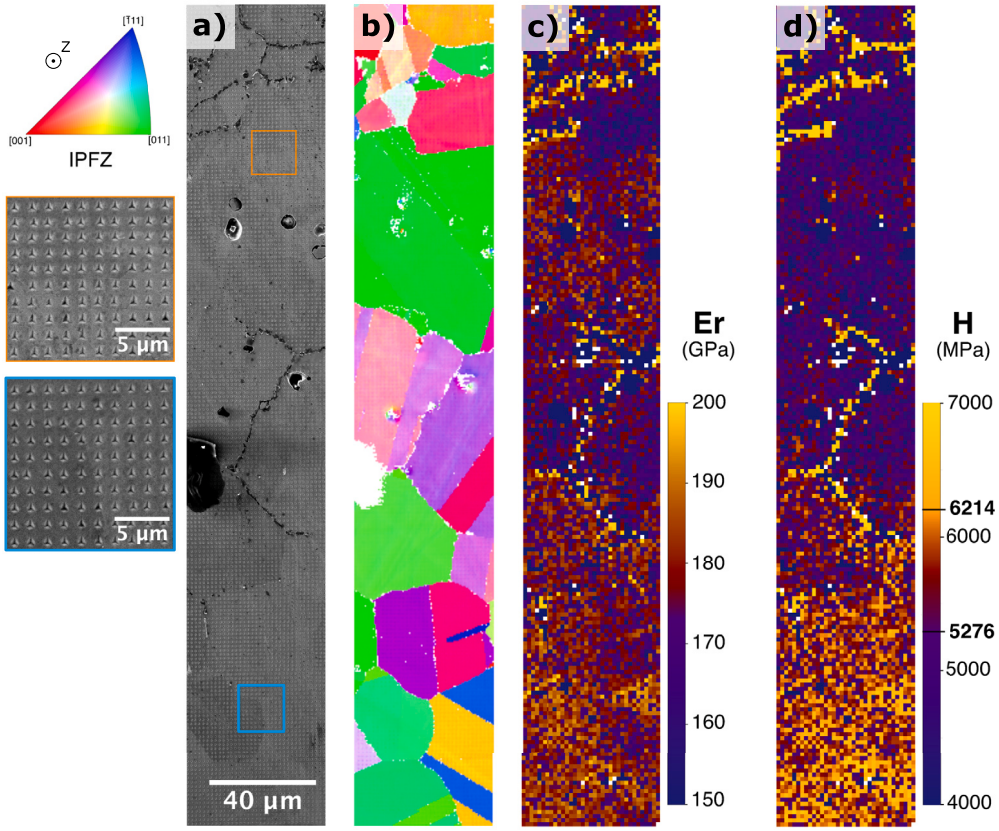

Fig. 4. Mechanical characterization of the chemical gradient by nanoindentation mapping: high speed nanoindentation mapping (HSNM). (a) SEM micrograph of the indented area with (b) the corresponding EBSD. Magnifications show the constant size of the indents obtained by the displacement driven mode. (c) Reduced modulus (*Er*) map. (d) Hardness (*H*) map. Bold values on the hardness colorbar correspond to the mean hardness values within the magnified areas.

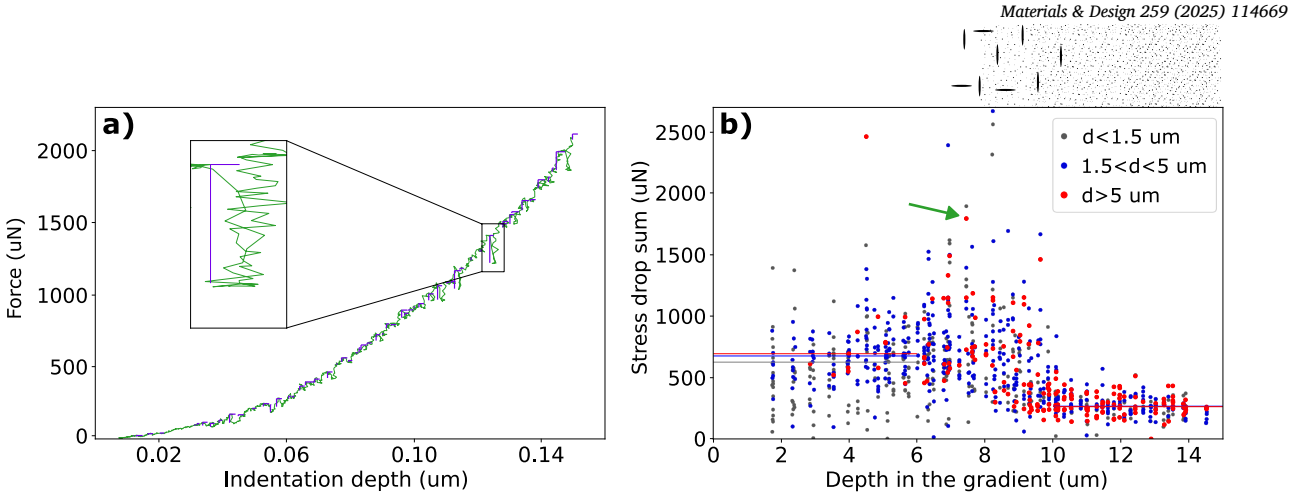

Fig. 5. Stress-drop analysis on indentation curves. a) Indentation curve of a single stress-drop-like test (pointed by the green arrow on the b) plot) with the identified stress drops. b) Sum of the stress-drop for each tests as a function of their depth in the gradient (distance to the original surface, before wedge-cut polishing). Points are classified depending on their distance d with a grain boundary or an oxide particle. Horizontal lines correspond to average values in the 0-6 μm and 10-14 μm depth ranges.

strain curves. The same plot also shows different trends depending on the position of the indents in the chemical gradient (recalled in the top of the Fig. 5(b)). In average, the amount of stress drop amplitude is larger in the precipitation-free region than in the γ'' precipitation-dense area. This observation can be made on the 3 categories mentioned above. One can also note that the points scattering is much larger in the precipitation-free area. In the transitional region of the graded microstructure, points are heavily scattered and some of them have a higher amount of stress-drop amplitude than both precipitation-free and precipitation-dense area.

In order to investigate the origin of the stress-drops, the sample surface was examined after the indentation. SEM micrograph of selected indents along the chemical gradient are depicted in Fig. 6. Slip bands can be observed near the indent marks and the furthest slip bands from the indent are pointed by the arrows. On one hand, the slip band intensity captured at the surface of the sample does not seem to be related to the amount of stress-drop. Indeed, indents #1, #4, #7, and #13 exhibit higher intensity slip bands as compared to indents #3, and #9; but are not necessarily the ones which have the higher amount of stress-drop amplitude. In addition, surface analysis of indent #3 – which has an amount of stress-drop amplitude much higher than the others – does not show a singular behavior compared to the other indents. On the other hand, it seems that in the γ'' precipitation-dense region, slip bands are closer from the indent than the ones in the precipitation-free region. The observations made on the indents presented on Fig. 6 were also made at a larger scale, on tens of indents spread over the gradient and different crystallographic orientations. However, even with the large number of indents studied, the observations made could be influenced by the grain and tip orientations and the corresponding Schmid factors associated with the triaxial nanoindentation test.

3.3. Micro-pillar compression tests

A total of 27 micro-pillar compression tests were performed over the gradient on sample #2 (it is worth reminding that the oxidation-affected region is deeper for sample #2 compared to sample #1 due to longer exposure at high temperature). Compression tests performed within the same grain are very repeatable, as shown later in Fig. 9. A selection of compression curves representative of each cluster of micro-pillars is shown in Fig. 7. Each stress-strain compression curve has a specific color code in accordance with the schematic of the wedge-cut sample:

- A precipitation-free region.
- A transitional region. At the top of this region (•) it is less likely to encounter γ'' precipitates but δ can be encountered. However, the distance between δ precipitates can be larger than the pillar size. The amount of δ within a pillar is very variable from pillar to pillar. At lower (•), there is a higher density of γ'' precipitates. At the bottom (•), even less δ phases can be found but the density of γ'' precipitates increases.
- A precipitation-dense region corresponding to the homogeneous bulk material, *i.e.*, the material not affected by the oxidation.

The stress-strain compression curves in Fig. 7 reveal that both the yield strength and the hardness increase with the depth of the micro-pillar position in the gradient. In other words, the denser the γ'' precipitation, the higher the yield strength. Other differences between the compression curves can be observed as well, such as the amount of stress-drops, their amplitude and the strain-hardening rate. These features will be discussed later in this article.

The grain orientation information obtained from EBSD characterization was used to identify the active slip plane corresponding to the slip traces at the pillar surfaces. In all the cases studied, the active slip plane is the slip plane with the highest Schmid factor. Thus, the active slip system was considered as the slip system with the highest Schmid factor for the corresponding slip traces. The highest Schmid factor was then used to evaluate the critical resolved shear strength using the following equation:

$$\tau_{CRSS} = \sigma_c.m$$

where σ_c is the stress at which the first slip band is triggered and m is the Schmid factor of the active slip system. The first active slip system was identified thanks movies taken *in-situ* during the tests.

The CRSS values obtained from each compression test were plotted as a function of the position in the gradient (Fig. 8). Results show that the denser the γ'' precipitation, the greater the CRSS. Indeed, two clusters can be pointed out: micro-pillars in the γ''- free region (position below 0.35 μm) have CRSS values lower than 380 MPa whereas micro-pillars in the γ''- dense region (position above 0.35 μm) have CRSS values higher than 380 MPa. This cluster analysis was preferred to the linear tendency which is associated to a poor coefficient of determination ($r^2 = 0.78$).

When focusing on the slip activity during the compression test, a few examples from both the γ'' precipitation-free area and the γ'' precipitation-dense regions can be emphasized. These examples are shown in Fig. 9. Pillars A and B are located in the γ'' precipitation-free region and are associated with a low yield stress, as observed

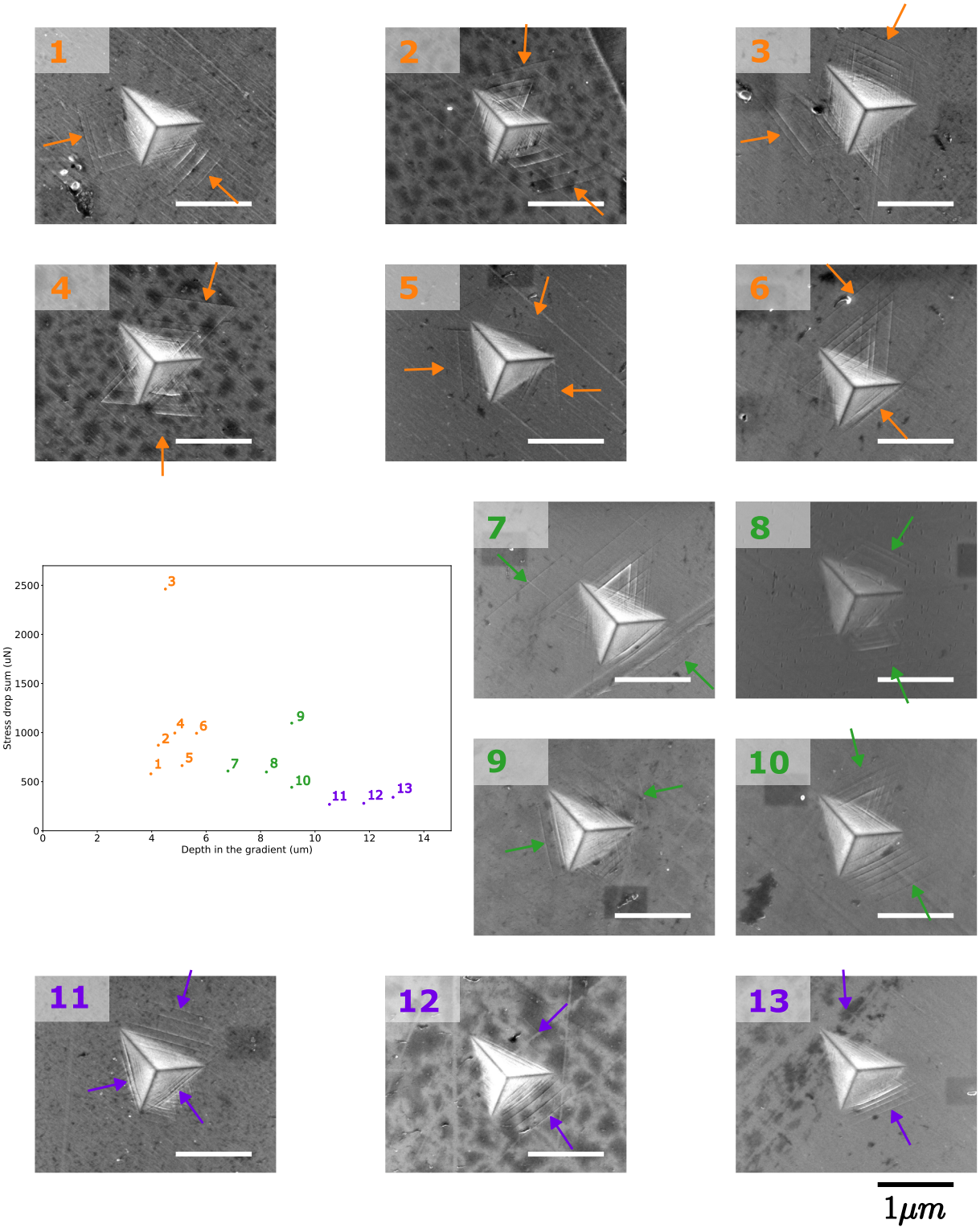

Fig. 6. Surface analysis of selected indents along the chemical gradient. Colors refer to the position in the gradient and are recalled on the sum of the stress-drop plot. Arrows are pointed at the furthest slip band from the indent.

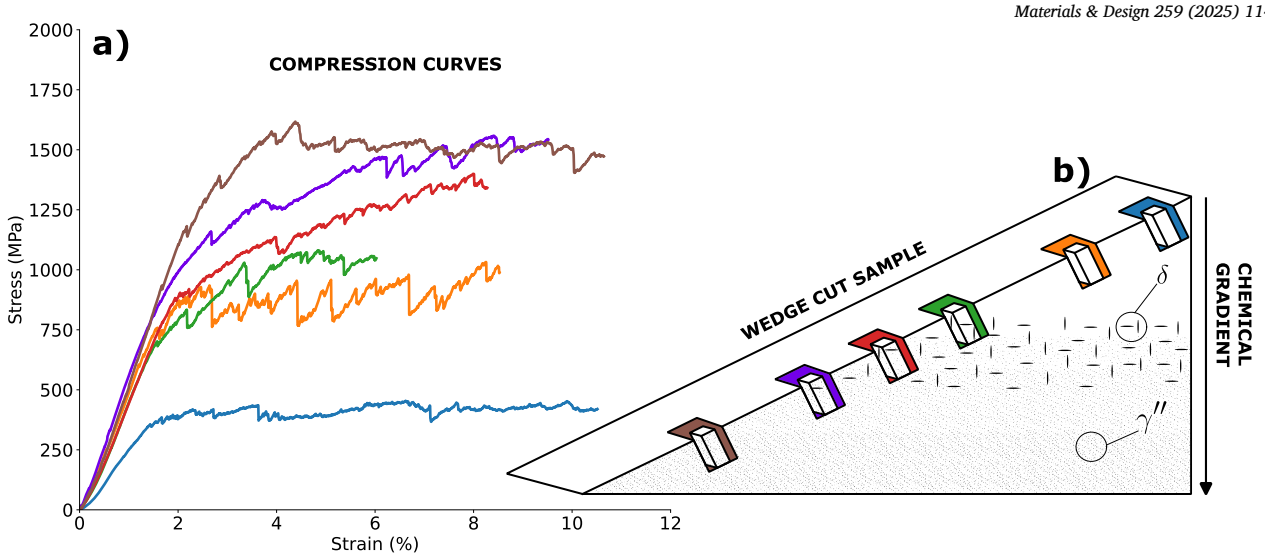

Fig. 7. (a) Stress-Strain compression curves of a few representative tests performed in the chemical gradient. (b) Schematic illustration of the location of the pillars in the chemical gradient and description of the associated colorcode. Pillars on the drawing are linked to the curves by their colors.

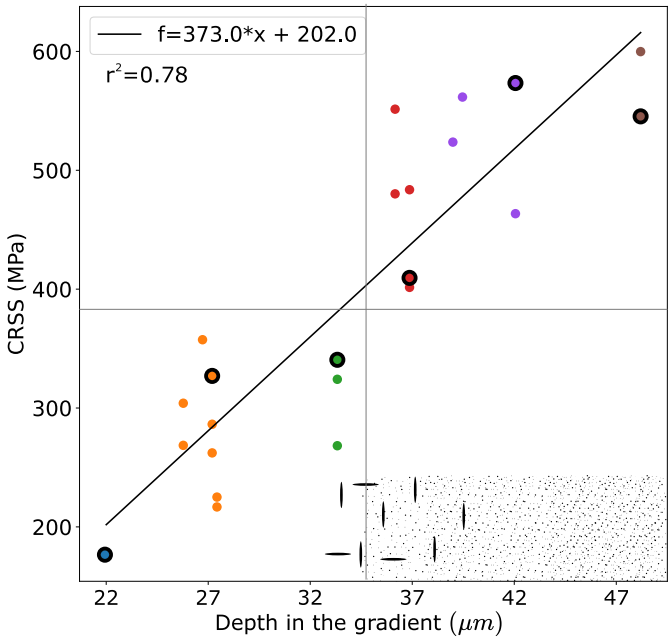

Fig. 8. Critical resolved shear stress (CRSS) of each micro-pillar plotted as a function of their position in the chemical gradient. Colors refers to the position in the different regions tested in the chemical gradient. Points resulting from the compression tests shown in Fig. 7 are surrounded.

on the compression curves (Fig. 7). One can notice that compression curves are surprisingly repeatable within each region given the scatter often observed with this type of tests. Pillar A exhibits intense slip bands along 2 slip systems, perfectly symmetric and with slip bands concentrated in only a few tens of nanometers. Pillar B demonstrates slip bands which are much less intense and spaced further apart, as depicted in the insert micrograph on the pillar side for brightness/contrast enhancement. Looking at the pillars in the γ'' precipitation-dense region, Pillar C presents shallow bands that are close together. Conversely to Pillar A, slip bands are spread all over the height of the pillar. Pillar D has fewer but more intense slip bands than Pillar C. These bands are also spaced further apart. In brief, no slip band typology trend according to the precipitation state can be drawn from these micro-pillars compression tests, *i.e.*, for monocrystalline pillars. While a clear difference of yield strength can be observed between the two regions, no trend in the occurrence and intensity of stress-drop can be drawn from these tests.

Further investigations were conducted on the characterization of the stress-drops occurring during micro-pillar compression, similarly to conventional nanoindentation. Fig. 10 is a summary of these findings. It is worth noting that not all tests were performed on the same crystallographic orientation. However, points vertically aligned in Fig. 10 come from micro-pillars milled in the same grain. For each compression test, stress-drops were identified in each compression curve and their stress amplitude was collected. In Fig. 10, the stress-drop amplitudes were summed below 3.5 % of plastic deformation and are plotted for each compression test as a function of the position within the gradient. No significant differences can be observed between the precipitate-free and precipitate-dense regions. Within the same grain, the amount of stress-drop can significantly vary (double or more) between indentation curves.

The number of active slip systems and the strain-hardening parameters are also indicated in Fig. 10 as marker shape and color variation, respectively. The number of active slip systems has been identified thanks to the SEM images and video acquired *in-situ* during the compression tests and the EBSD data. Most compression tests activated 2 slip systems. Only 3 tests (out of 23) in the precipitate-free region activated only one slip system. 2 of these tests show a really low amount of stress-drops. For some compression tests, 3 slip systems were activated instead of 2 slip systems. In these cases, the amount of stress-drops was lower than any other tests with 2 active slip systems. In addition, the number of active slip systems does not influence the strain-hardening since widely spread strain-hardening values can be found for each category of number of active slip systems. Moreover, the strain-hardening and the amount of stress-drops do not seem to be correlated as, once again, widely spread strain-hardening values can be found in both high sum of stress-drop region (>600 MPa) and low sum of stress-drop region(<400 MPa).

One specific configuration – corresponding to the case A depicted in Fig. 9 – shows a significantly higher sum of stress-drops (>850 MPa) than the other tests. These micro-pillars are located in 2 different grains but with the same crystallographic orientation. One explanation to this behavior could be a microstructural/chemical heterogeneity within the micro-pillars. As these micro-pillars are close to the transitional region (with δ precipitation) and because of the wedge-cut sample technique, δ precipitation could be found at the bottom of the pillar. This would lead

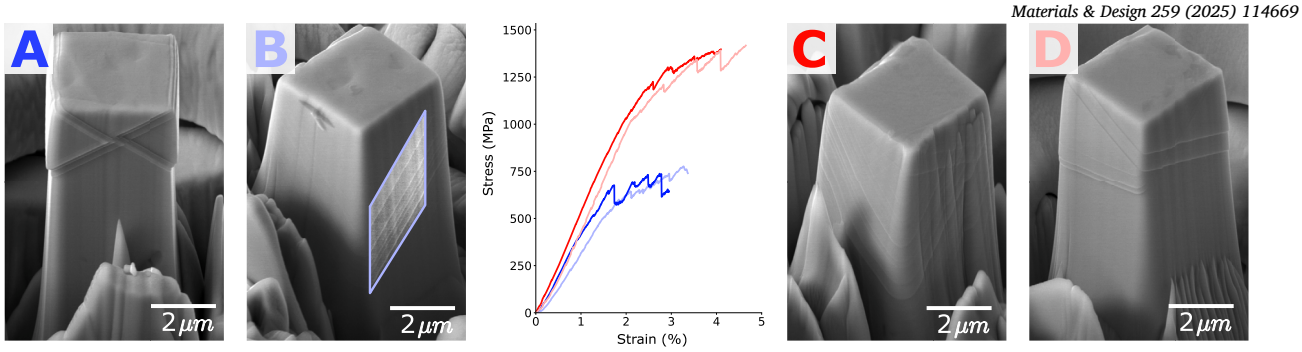

Fig. 9. SEM micrographs of 4 different micro-pillars after compression at a strain level between 1 and 2 % of plastic deformation. Pillars A and B are located in the γ'' precipitation-free area and their compression curves are plotted in shades of blue. Pillars C and D are located in the γ'' precipitation-dense area and their compression curves are plotted in shades of red.

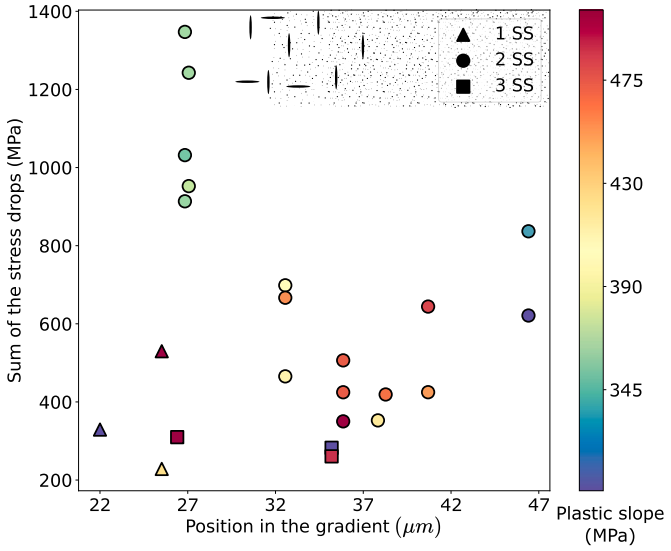

Fig. 10. Sum of stress-drop amplitude measured on compression curves below 3.5 % of plastic deformation. Each point corresponds to a pillar and is plotted as a function of its position in the chemical gradient. Points shapes corresponds to the number of active slip systems (SS) and colors indicates the strain-hardening measured during compression tests.

to a stress concentration in the upper part of the pillar and an intense slip localization.

3.4. High resolution-digital image correlation (HR-DIC) under tensile loading

Interrupted tensile tests paired with HR-DIC technique was conducted to document the evolution of the slip localization at the sub-grain level in the precipitation-hardened (sample #4) and the solid-solution Alloy 718 (sample #3). These metallurgical states correspond to the bulk material and the oxidation-affected region within the pre-oxidized specimen, respectively. Three deformation steps were considered up to 1.8 % of plastic strain. The EBSD and strain maps associated to the investigated regions are shown in Figs. 12 and 11 for the solid-solution and precipitation-hardened specimens, respectively. Both samples are presenting similar grain structure. Both materials display plastic localization in the form of concentrated strain bands (*i.e.*, slip localization: strain concentration due to slip band) with different slip localization amplitude and spatial distribution from one metallurgical state to the other. The active slip systems are systematically the systems with the highest Schmid factor which is in agreement with the observations made on micro-pillars compression tests and HR-DIC experiments under tensile loading. The solid-solution Alloy 718 (Fig. 12) exhibits a higher density of localized bands of lower amplitude compared to the precipitation-hardened Alloy 718 (Fig. 11). As show in Figs. 12(g) and 11(g), the precipitation-hardened Alloy 718 displays less localized bands but they are significantly higher slip amplitude (in-plane slip amplitude ranging up to 170 nm at 1.26 % of plastic strain) compared to the solid-solution Alloy 718 (in-plane slip amplitude ranging up to 60 nm at 1.81 % of plastic strain).

A statistical analysis of the slip band distribution and amplitude (amplitude of strain induced by individual slip band) was carried out on both the metallurgical states of the Alloy 718. The results are summarized in Fig. 13. The maximum slip amplitude (along the band) normalized by the length of the slip band increases as a function of the macroscopic plastic strain for both metallurgical states (Fig. 13(a)). For each loading step, the maximum slip amplitude is significantly greater for the precipitation-hardened state compared to the solid-solution state. The slip bands of the precipitation-hardened Alloy 718 are also more spaced as shown in Fig. 13(b), confirming the heterogeneous strain distribution observed on strain maps. In this plot, the slip band spacing was measured across several crystallographic grains, and each data point represents the average slip band spacing as a function of the average maximum slip amplitude of all bands within a given grain. Moreover, in the case of the solid-solution Alloy 718, the amplitude of the slip localization events increases only slightly with increasing plastic deformation. In contrast, the amplitude of events in the precipitation-hardened Alloy 718 increases significantly with increasing plastic deformation.

These statistical results show that the solid-solution Alloy 718 presents a high density of low amplitude slip bands, whereas the precipitation-hardened alloy shows significantly more intense bands. These slip bands are more spaced and therefore less numerous per grain.

4. Discussion

The present paper benchmarked different micromechanical testing techniques generally used to probe the crystal plasticity character of materials at the sub-grain scale. It is worth noting that both the nanoindentation and micro-pillar compression tests are used here to assess the mechanical response of the material in a “monocrystalline” material while the HR-DIC technique under tensile loading is used to probe the deformation capability of a polycrystalline aggregate. The elastic anisotropy in the Alloy 718 [42] can favor strain concentration and participate in the intensity and distribution of the slip localization events [49,20]. Both nanoindentation and micro-pillar compression tests present the advantage of having an exploitable stress-strain curve representative of the tested grain, the mechanical response being highly sensitive to the precipitation state. However, the stress-drop analyses and slip trace identification on pillars and from nanoidentation tests were more a case-by-case response with no important trends related to the metallurgical state, despite a macroscopic yield strength three times greater for the precipitation-hardened Alloy 718 compared to the solid-solution

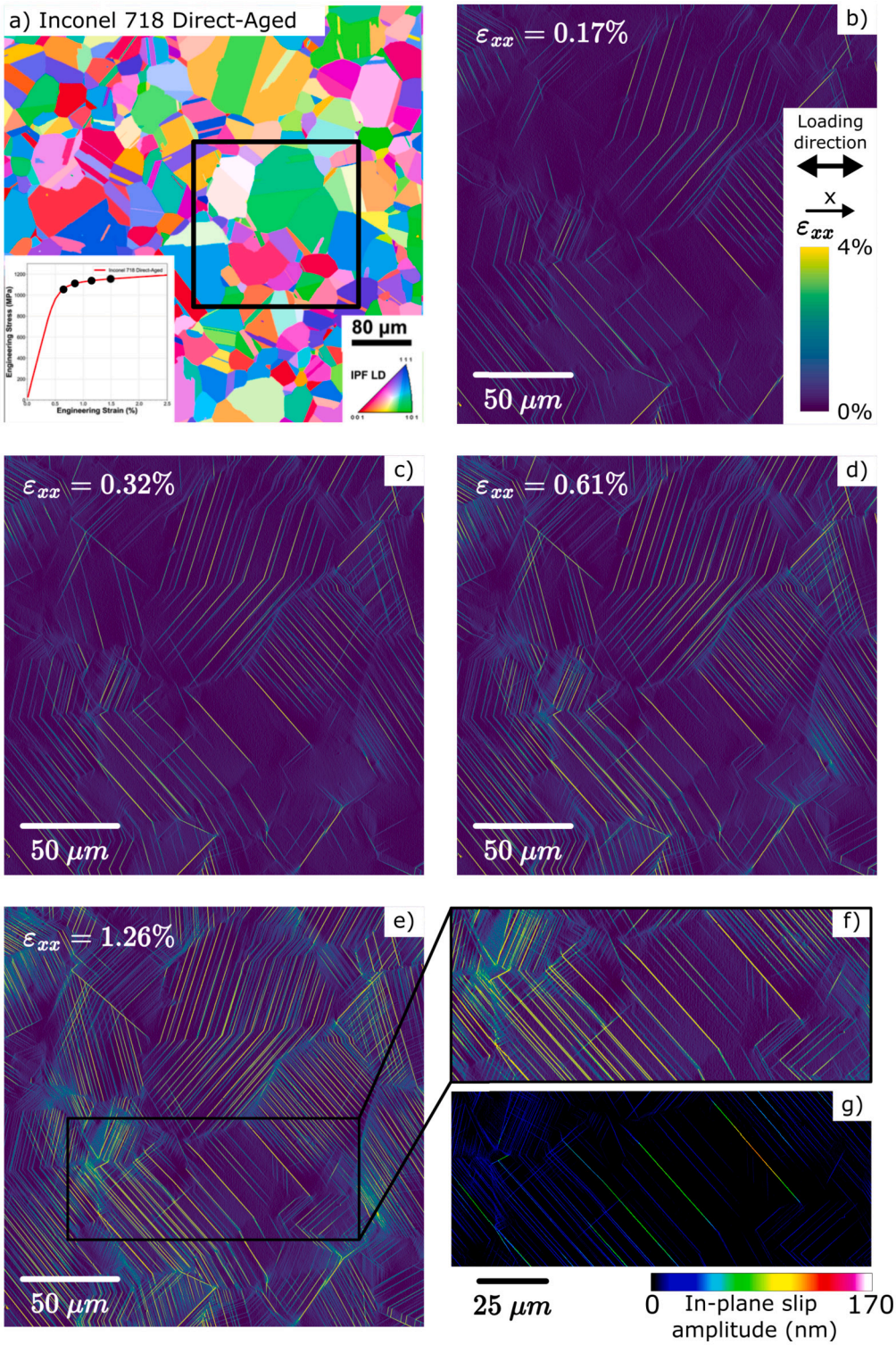

Fig. 11. Sub-grain deformation map of the precipitation-hardened Alloy 718. (a) EBSD map with inverse pole figure represented along the loading direction. The associated tensile curve with interruptions is plotted as an insert. Full strain field along the loading direction at approximately (b) 0.17 %, (c) 0.32 %, (d) 0.61 %, and (e) 1.26 % plastic strain. (f) Magnification of the strain field (e). (g) In-plane slip amplitude map obtained by the Heaviside-DIC method.

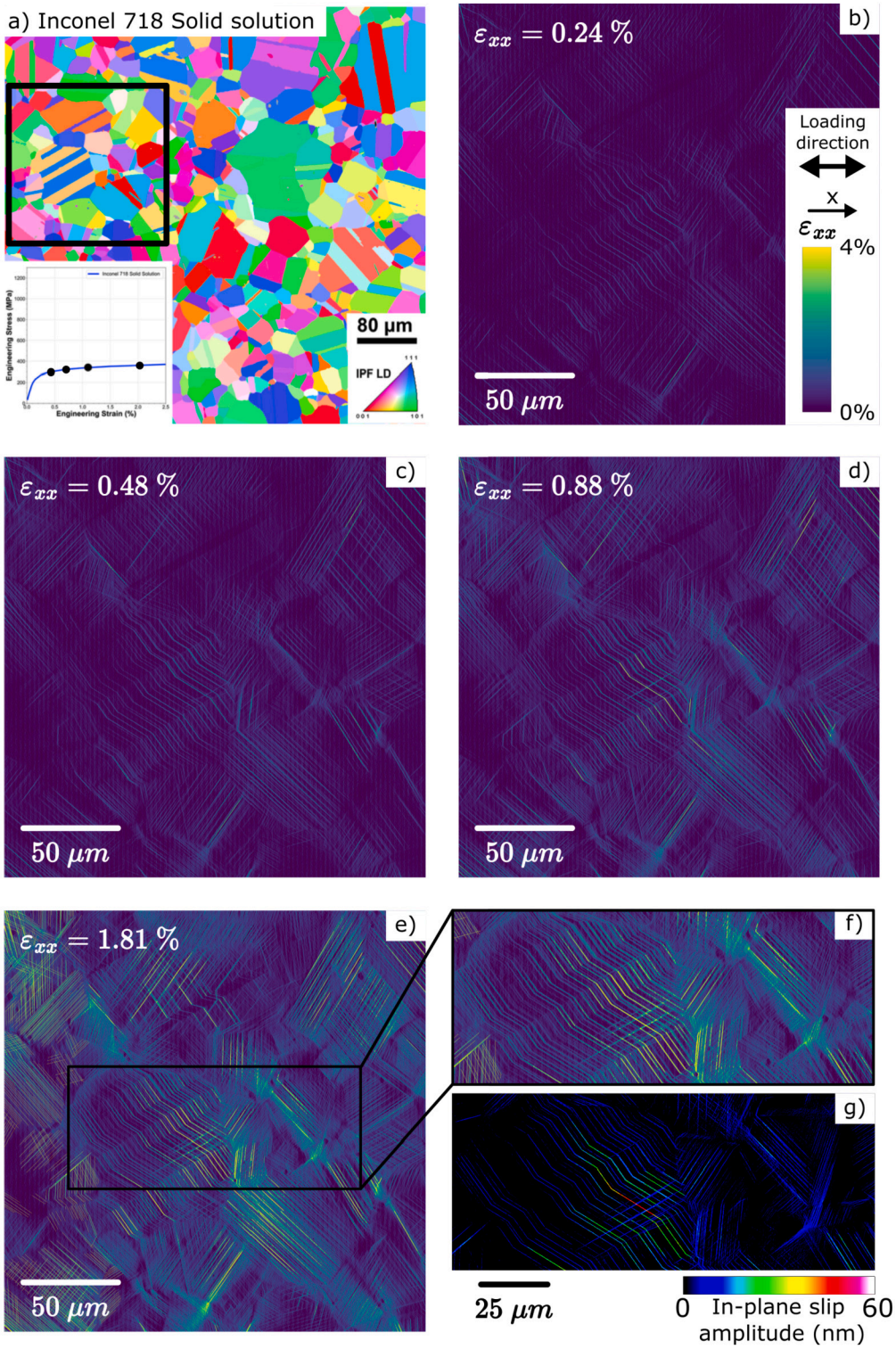

Fig. 12. Sub-grain deformation map of the solid-solution Alloy 718. (a) EBSD map with inverse pole figure represented along the loading direction. The associated tensile curve with interruptions is plotted as an insert. Full strain field along the loading direction at approximately (b) 0.24 %, (c) 0.48 %, (d) 0.88 % and 1.81 % plastic strain. (f) Magnification of the strain field (e). (g) In-plane slip amplitude map obtained by the Heaviside-DIC method.

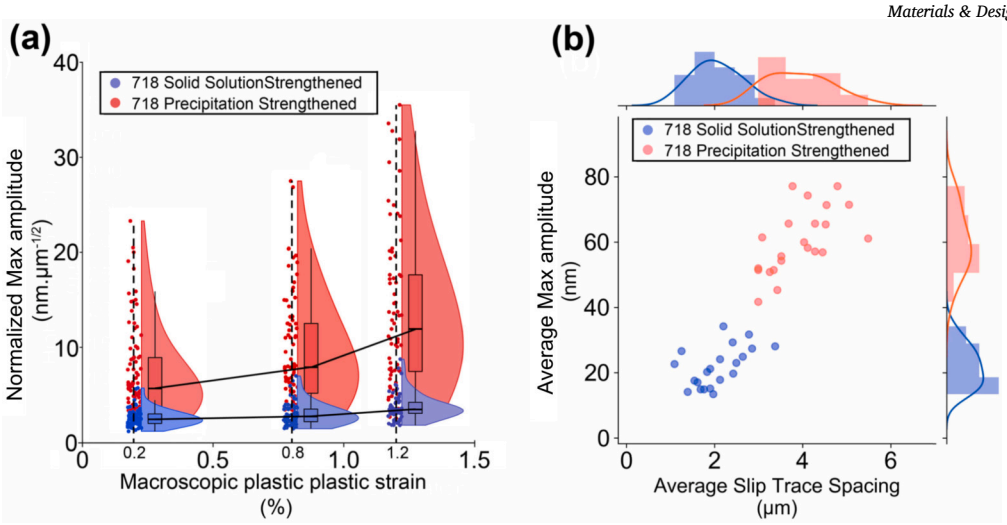

Fig. 13. Statistical analysis of results obtained by high resolution-digital image correlation. (a) Maximum slip amplitude normalized by the slip length for the precipitation-hardened (sample #4) and the solid-solution Alloy 718 (sample #3) as a function of the macroscopic plastic deformation. (b) Average max amplitude (per crystallographic grain) as the function of average slip trace spacing for the precipitation-hardened (sample #4) and the solid-solution Alloy 718 (sample #3).

Table 1
Comparison of the compressed pillars shown in Fig. 9. Sol^2 stands for solid-solution and PH for precipitation-hardened.

	A	B	C	D
Grade	Sol^2	Sol^2	PH	PH
Number of active Slip Sytems	2	1	3	2
Schmid factors	0.425 ; 0.404	0.459	0.475 ; 0.389 ; 0,378	0.465 ; 0.415
CRSS (MPa)	274	272	579	560
Slip bands distribution	Intense & Close	Shallow & Far	Shallow & Close	Intense & Far

Alloy 718. The HR-DIC technique is not capable to assess the local stress response of the material but evidenced a very distinct strain localization response in the Alloy 718 depending on its precipitation state. Based on the main results of the present investigation, different points will be discussed in the following sections, such as slip localization and stress-drop analyses as well as technical advantages and drawbacks to inform on the crystal plasticity behavior at the sub-grain level.

4.1. Slip band distribution analysis

The slip activity of both the precipitation-hardened and solid-solution Alloy 718 was investigated using HR-DIC, micro-pillar compression and nanoindentation. Whereas the HR-DIC clearly shows differences in slip band spatial distribution and amplitude between both Alloy 718 grades, micro-pillar compression and nanoindentation did not converged to the same results. From the HR-DIC results at less than 2 % of macroscopic plastic deformation, the precipitation-hardened grade exhibits intense slip bands highly spaced apart. In comparison, the solid-solution grade presents less intense slip bands and closer together. This result on the strain localization intensity and density is in good agreement to the conclusions of Harte et al. [18] performing HR-DIC on different Ni-based superalloys either in a solid-solution state or precipitation-hardened state. Micro-pillar compression in the solid-solution region of the graded Alloy 718 showed that both intense slip bands close from each other and shallow slip bands highly spaced apart can be found. The same observation has been made in the precipitation-hardened region of the graded Alloy 718. Therefore, the characterization of the spatial distribution of slip bands and strain localization intensity using micro-pillar is not trivial to further predict the strain localization character of polycrystalline aggregates under tension.

In order to better understand the differences in slip amplitude and slip band distribution between the pillars, findings made on the micro-pillars examples depicted in Fig. 9 have been summarized in Table 1. First, the CRSS values in the solid-solution region (precipitation-free) is very similar for both micro-pillars A and B (274 and 272 MPa, respectively), but the micro-pillars have very different slip band distribution; micro-pillar A showing intense slip bands close from each other while micro-pillar B shows shallow slip bands highly spaced apart. The same observation can be done on the micro-pillars C and D in the precipitation-hardened region. Thus, the CRSS is not responsible for this diverging slip activity while HR-DIC clearly evidenced clear tendencies on polycrystalline aggregates. Likewise, the number of active slip systems does not seem to influence neither the slip band spatial distribution nor their amplitude, as observed in Fig. 10. However, the crystallographic orientation and the resulting Schmid factors might have an impact on the slip band amplitude. From Table 1, pillars activating 2 slip systems with 2 close Schmid factors (pillars A and D) show a high slip amplitude compared to the other 2 pillars. In that case, the slip activity would depend more on the crystallographic orientation than on the precipitation density. Changes in slip activity due to precipitation density may be hindered by the effect of crystallographic orientation.

The analysis of the slip bands at the surface of the sample tested by conventional nanoindentation showed a slighly different response compared to micro-pillar compression. Indeed, slip bands were found further from the center of the indent in the precipitation-free region compared to the γ'' precipitation-dense region. As the yield strength is higher in the precipitation-dense region, it witnesses a size difference between the plastic volume probed for both the metallurgical states. Even if displacement-driven tests ensure the same penetration depth regardless of the reduced modulus and hardness of the material, the volume probed during the indentation test differs depending on the grain orientation due to the elastic anisotropic response of the material and the yield strength related to both the grain orientation and precipitation state. Therefore, the non-constant plastic volume probed during nanoindentation tests complicates the slip activity analysis, being opposite in terms of slip band spacing.

This affected plastic volume could be an explanation to the different slip activity captured by HR-DIC and micro-pillar compression. Indeed, the plastic response measured by HR-DIC is a complex response of the entire microstructure: the plastic response of individual grains, the plasticity development from stress concentration from grains to grains due to elastic anisotropy but also the effect of the plasticity confinement by the grain boundaries. It can manifest as an hardening described by the Hall-Petch relationship or as interactions between slip bands and grain boundaries such as micro-volumes [68,26]. Conversely, the plasticity is not confined by grain boundaries when testing a single crystal. The micro-pillar compression technique probes a given volume with many free surfaces. Therefore, slip bands easily escape at the free-surfaces. Thus, the confinement of the plasticity by the grain boundaries could explain the different slip activity responses captured by HR-DIC and micro-pillar. This emphasizes the need for methods employing large fields of views, such as HR-DIC, to describe the representative slip activity at the part scale in Alloy 718. Furthermore, Zhao et al. [69] have also evidenced different dislocation structures within micro-pillars due to size effect in micrometric pillars. Therefore, additional dislocation structure characterizations using TEM would support and complement surface observations via slip trace analyses.

4.2. On the origin of the stress-drops

Stress-drop analysis was carried out on both the conventional nanoindentation results and micro-pillar compression. As mentioned above, the slip band analysis performed post-mortem after conventional nanoindentation showed a difference in plastic volume affected by the indentation between the precipitation-free and precipitation-dense regions. In that specific case, the γ'' precipitation limits the dislocation movement and thus confines the plasticity. The fact that a lower amount of stress-drop is observed in the γ'' precipitation-dense region could indicate that stress-drops are more likely related to slip bands emergence to the surface. Indeed, if stress-drops were related to precipitation shearing, a higher amount of stress drop would be observed in the γ'' precipitation-dense region. Instead, a higher amount of stress drop was found with a greater number of slip bands for the solid-solution state. However, the fact that the plastic volume affected is different between the solid-solution region to the precipitation-hardened region makes it difficult to conclude on the differences in plastic behavior between the two regions. In addition, the complex mechanical loading associated with the shape of the tip used (Berkovich) makes the plastic response dependent on the crystallographic orientation. In the perspective of pushing forward into the high-throughput identification of the plastic mechanisms responsible for stress-drops on indentation curves, the use of a spherical or spheroconical tip might limit discrepancy in plastic response for a given grain orientation. One could also consider performing some indentations at a larger scale to capture a homogenized mechanical response of several grains, leveling the mechanical response over a larger volume.

The micro-pillar compression technique leads to the confinement of plasticity within a known volume, *i.e.*, the pillar size. Even so, the stress-drop analysis results in a number of parameter pairs that cannot be correlated (see Fig. 10). First, in the present study as well as others in the literature [70], no relationship could be established between the occurrence of a single stress-drop and the emergence of slip bands at the surface of a pillar. Also, no correlation was found between the slip band amplitude and neither the amount of stress-drop amplitude nor their number. Detailed examples to support this statement can be found in the supplementary material. Second, it was found and shown in Fig. 10 that the precipitation state does not influence the amount of stress-drop amplitude, which supports the hypothesis made with conventional nanoindentation. Third, some studies have found that the activation of several slip systems could lead to less work-hardening compared to a single slip configuration [71]. In the present study, no correlation was found between the number of active slip systems and the work-hardening. Finally, most micro-pillars show multiple active slip systems with only 3 pillars activating a single slip system. For the two pillars located at 26 μm in the gradient (solid-solution state), this can be explained by the significant difference between the first and second Schmid factor (~0.12). As for the pillar located at 22 μm within the gradient (solid-solution state), difference between the first and second Schmid factor is smaller (0.03) but the first Schmid factor is of 0.498. This very favorable grain orientation for slip activity could be responsible for the concentration of the slip in a single slip system. In comparison, when soliciting the entire microstructure, HR-DIC measurements revealed very few secondary slip activity in both the precipitation-strengthened and solid-solution Alloys 718. Again, this might be related to the lack of plasticity confinement by the grain boundaries with micro-pillar compression which makes easier the activation of a second slip system.

4.3. Technique confrontation

Several micro-mechanical techniques were used in the present study to characterize the mechanical response of a chemically-graded material. Advantages and drawbacks identified in this study are listed in Table 2.

Nanoindentation mapping combined with a wedge-cut polishing technique was found to be a good solution to quickly access the local mechanical properties of the gradient, especially when its depth extension corresponds to the distance of few indents on a conventional cross-section. The main technical challenge of this test is to isolate the very stiff and sensitive MEMS sensor from external vibrations. The sample preparation, despite delicate for wedge-cut preparation, requires low skills and access to common metallographic preparation techniques (polishing). It makes nanoindentation very appealing for high-throughput data collection to describe the heterogeneous mechanical response of materials at the grain/phase level. Nevertheless, nanoindentation technique remains very sensitive to surface preparation. The wedge-cut polishing of pre-oxidized samples, as careful as it was, is more complicated than conventional surface preparation techniques and can induce slight scratches at the sample surface due to oxide particles detaching from oxidized grain boundaries or external oxide layer. Such surface preparation artifacts can add noise on the measured mechanical properties and thus affect the evaluation of the elastic anisotropy of the tested material. Increase in nanoindentation speed with a pretty good positioning and sensitivity (force and displacement) allows for high speed nanoindentation mapping with high resolution to probe the local mechanical properties at the micron/submicron scale [37,39,38,31,42]. High resolution nanoindentation mapping can be obtained, allowing to differentiate small size phases such as an oxidized grain boundary, or accurately characterize the hardness and reduced modulus evolution along the gradient [31,59]. Despite inverse methods are very effective to assess anisotropic elastic properties from reduced modulus maps [31,42,72,73], the full exploitation of hardness properties to identify the crystal plasticity response is not direct. In addition, local load-displacement curves obtained by conventional nanoindentation also provide information about the plastic activity in the gradient (pop-in/stress-drop). However, the mechanical loading complexity and the non-confinement of the plasticity, *i.e.*, increasing indented volume with depth make it difficult to identify the origin of plastic activity and/or compare the plastic activity between different regions of the gradient. In addition, nanoindentation is also prone to size effect due to the effect of activation sources and plasticity development.

The micro-pillar compression also allows to assess small regions within the gradient – with resolution 10 times greater than nanoindentation – to extract stress-strain curves. The set-up phase is more complex, longer and more sensitive to manufacturing as mentioned in the introduction [74–76]. FIB-machining artifacts are well described in the literature and can affect the mechanical response of small-size pillars. Gallium implantation and irradiation hardening, surface curtaining

Table 2
Techniques advantages and drawbacks for the gradient characterization.

	Nanoindentation	Micro-pillar compression	HR-DIC
Advantages	- Easy to set up	- Confinement of the plasticity	- Global mechanical response of the microstructure
	- Probing very small volumes (high resolution)	- Allow to isolate microstructural features	- Statistically presentative dataset
	- Local stress-displacement curves	- 3D characterization of plastic mechanisms	
		- Local stress-strain curves	
Drawbacks	- Complex mechanical loading	- Sensitive to size effect and manufacturing	- 2D information
	- Difficulties to access the information on plastic mechanisms		- No local stress-strain curves

effects, edge blunting, taper angles, etc., are common issues encountered during FIB-machining. In this study, all the pillars were machined following the same semi-automatic method, leading to similar artifacts from pillar to pillar. For instance, Fig. 9 showed stripes parallel to the loading direction at the surface of some pillars (curtaining effect) and slight variations in the taper angles. However, based on the repeatability of the elastic behavior of the pillar and the trend of the CRSS, the surface preparation artifacts were found to have very little influence on the mechanical properties compared to the contribution of the metallurgical state. Compared to nanoindentation, micro-pillar compression allows to probe a known volume with much easier stress state to consider. The plastic volume affected during the micro-pillar compression test is identical for all pillars independently on the their position in the gradient. Plastic responses are then comparable between tests and the emergence of plastic events on the different pillar surfaces allows for identifying the active slip systems and characterize slip activity. However, the relationship between the stress-drop observed on the local stress-strain curves and the slip activity – slip amplitude and slip distribution – remains unresolved. Therefore, it is impossible to predict the slip activity from the local stress-strain curves as well as the slip localization character, *i.e.*, slip intensity and spatial distribution.

While micro-pillar compression isolates a single crystallographic orientation (in this study) or microstructural feature to measure its response to a compression loading, HR-DIC captures the mechanical response of a polycrystalline aggregate. Both information are complementary. Comparing the results of both techniques in the present study, allowed to found out that the slip activity is different whether the deformation was confined by the grain boundaries or not, potentially due to the elastic anisotropy and grain deformation incompatibility leading to complex stress-strain fields in polycrystalline aggregates.

5. Conclusions

In the present work, a framework has been developed to create and test material with a gradient of chemical composition/microstructure/properties over tens of micrometers. The wedge-cut preparation technique paired with nanoindentation mapping was found to be a good combination to characterize the hardness gradient associated with the γ'' precipitation depletion with high spatial resolution in a Ni-based 718 alloy. The increase in local yield strength and CRSS with the increasing density of γ'' precipitates was also quantified along the chemical gradient thanks to micro-pillar compression. The plastic response and slip activity were found to be significantly different between a polycrystalline aggregate and a single orientation. Indeed, no relationship can be established between the plastic activity identified by micro-pillar compression or nanoindentation and the γ'' precipitates density while tensile testing paired with HR-DIC showed that slip bands are more intense and spaced farther apart in a γ''-dense region compared to a γ''-free region. This emphasizes the role of intragranular slip localization and the contribution of neighboring grains on the slip activity, intensity and spatial distribution in polycrystalline aggregates. The HR-DIC is a particularly appropriate technique to characterize the slip localization behavior of polycrystalline aggregates but lacks in local quantitative stress-strain evaluation compared to nanoindentation and micro-pillar compression testing.

CRediT authorship contribution statement

Malo Jullien: Writing – original draft, Visualization, Software, Methodology, Investigation, Formal analysis, Conceptualization. **Marc Legros:** Writing – review & editing, Validation, Supervision, Resources, Methodology, Investigation, Conceptualization. **Mathieu Calvat:** Writing – review & editing, Visualization, Methodology, Investigation, Formal analysis, Conceptualization. **Jean-Charles Stinville:** Writing – review & editing, Visualization, Validation, Supervision, Resources, Project administration, Methodology, Investigation, Funding acquisition, Formal analysis, Conceptualization. **Damien Texier:** Writing – review & editing, Validation, Supervision, Resources, Project administration, Methodology, Investigation, Funding acquisition, Formal analysis, Conceptualization.

Funding

This research was funded, in part, by The European Research Council, project HT-S_4DefOx - Grant number 948007. A [CC-BY public copyright license] has been applied by the authors to the present document and will be applied to all subsequent versions up to the Author Accepted Manuscript arising from this submission, in accordance with the grant's open access conditions.

Declaration of competing interest

The authors declare the following financial interests/personal relationships which may be considered as potential competing interests: Damien TEXIER reports financial support was provided by European Research Council. Jean-Charles STINVILLE reports financial support was provided by National Science Foundation. Damien TEXIER reports financial support was provided by Centre National de la Recherche Scientifique. If there are other authors, they declare that they have no known competing financial interests or personal relationships that could have appeared to influence the work reported in this paper.

Acknowledgements

This work was supported by the European Research Council [project HT-S_4DefOx - Grant number 948007]. The authors are grateful to the *Centre National de la Recherche Scientifique (CNRS)* for the mobility grant with the International Research Project denoted "CIN&MAT". MC and JCS acknowledge the NSF (award #2338346) for financial support. This work was carried out in part in the Materials Research Laboratory Central Research Facilities at the University of Illinois Urbana-Champaign.

The authors particularly acknowledge the Raimond Castaing Microanalysis Centre (UAR 3623) for scanning electron microscopy access.

Appendix A. Supplementary material

Supplementary material related to this article can be found online at https://doi.org/10.1016/j.matdes.2025.114669.

Data availability

The raw/processed data required to reproduce these findings (manuscript and supplementary materials) cannot be shared at this time, as the data also forms part of an ongoing study. Data from the HR-DIC experiments are available through the DRYAD project platform [65,66].

References

[1] X. Tan, Y. Kok, Y.J. Tan, M. Descoins, D. Mangelinck, S.B. Tor, K.F. Leong, C.K. Chua, Graded microstructure and mechanical properties of additive manufactured Ti–6Al–4V via electron beam melting, Acta Mater. 97 (2015) 1–16, https://doi.org/10.1016/j.actamat.2015.06.036.

[2] Z. Ma, W. Liu, W. Li, H. Liu, J. Song, Y. Liu, Y. Huang, Y. Xia, Z. Wang, B. Liu, Z. Lv, G. Hu, T. Wang, T. Li, S. Liu, Y. Zhang, Additive manufacturing of functional gradient materials: a review of research progress and challenges, J. Alloys Compd. 971 (2024) 172642, https://doi.org/10.1016/j.jallcom.2023.172642.

[3] C. Zhang, F. Chen, Z. Huang, M. Jia, G. Chen, Y. Ye, Y. Lin, W. Liu, B. Chen, Q. Shen, L. Zhang, E.J. Lavernia, Additive manufacturing of functionally graded materials: a review, Mater. Sci. Eng. A 764 (2019) 138209, https://doi.org/10.1016/j.msea.2019.138209.

[4] V. Bhavar, P. Kattire, S. Thakare, S. patil, R. Singh, A review on functionally gradient materials (FGMs) and their applications, IOP Conf. Ser., Mater. Sci. Eng. 229 (2017) 012021, https://doi.org/10.1088/1757-899X/229/1/012021.

[5] X. Li, L. Lu, J. Li, et al., Mechanical properties and deformation mechanisms of gradient nanostructured metals and alloys, Nat. Rev., Mater. 5 (2020) 706–723, https://doi.org/10.1038/s41578-020-0212-2.

[6] E. Saly, P. Villechaise, D. Mellier, P. Sallot, A. Caradec, J. Cormier, Spark plasma sintering of nickel-based superalloys: a new route to produce dual-alloy turbine disks, in: The Minerals, in: Metals & Materials Series, Springer, Cham, 2024.

[7] J. Knörlein, M.M. Franke, M. Schloffer, T. Berger, C. Körner, Microstructure and mechanical properties of additively manufactured γ-TiAl with dual microstructure, Intermetallics 161 (2023) 107978, https://doi.org/10.1016/j.intermet.2023.107978.

[8] Z. Liu, M. Tang, Control of microstructure, defects and mechanical properties in direct energy deposited SS316L/Inconel 718 functionally graded material via mechanical vibration, Mater. Des. 242 (2024) 113010, https://doi.org/10.1016/j.matdes.2024.113010.

[9] C. Romain, D. Texier, C. Desgranges, et al., Oxidation of thin nickel-based superalloy specimens: kinetics study and mechanical integrity, Oxid. Met. 96 (2021) 169–182, https://doi.org/10.1007/s11085-021-10075-2.

[10] D. Texier, A. Palchoudhary, J. Genée, Q. Sirvin, Y. Zhang, G. Kermouche, D. Monceau, D. Poquillon, E. Andrieu, Effect of oxygen dissolution on the mechanical behavior of thin Ti-6Al-4V specimens oxidized at high temperature: experimental and modeling approach, Corros. Sci. 235 (2024) 112177, https://doi.org/10.1016/j.corsci.2024.112177.

[11] Q. Sirvin, J. Genée, B. Dod, D. Monceau, D. Texier, Oxygen ingress in titanium and its alloys after high-temperature oxidation: a competition between strengthening and embrittlement, Metall. Mater. Trans. A 56 (2025) 1858–1874, https://doi.org/10.1007/s11661-025-07737-0.

[12] J. Kang, Y. Liu, J. Zhou, W. Zhuo, J. Zhang, J. Zeng, H. Zhang, Y. Pei, S. Li, S. Gong, Temperature-dependent evolution mechanism of interface microstructure between gradient MCrAlY coatings and nickel-based superalloy, Mater. Des. 237 (2024) 112585, https://doi.org/10.1016/j.matdes.2023.112585.

[13] J. Zhang, S. Jiang, Y. Jia, P. Peng, Y. Li, S. Yang, Z. Lu, Microstructure evolution and hydrogen absorption characteristics of gradient-hydrogenated Ti-4.5Al-3V-2Mo-2Fe alloys, Mater. Des. 247 (2024) 113436, https://doi.org/10.1016/j.matdes.2024.113436.

[14] J. Ding, S. Xue, Z. Shang, J. Li, Y. Zhang, R. Su, T. Niu, H. Wang, X. Zhang, Characterization of precipitation in gradient Inconel 718 superalloy, Mater. Sci. Eng. A 804 (2021) 140718, https://doi.org/10.1016/j.msea.2020.140718.

[15] Y. Austernaud, M. Novelli, P. Bocher, T. Grosdidier, Effect of shot peening temperature on the microstructure induced by surface severe plastic deformation on an austenitic stainless steel, J. Mater. Process. Technol. 339 (2025) 118823, https://doi.org/10.1016/j.jmatprotec.2025.118823.

[16] E. Epifano, D. Monceau, Ellingham diagram: a new look at an old tool, Corros. Sci. 217 (2023).

[17] T. Sanviemvongsak, D. Monceau, C. Desgranges, B. Macquaire, Intergranular oxidation of Ni-base alloy 718 with a focus on additive manufacturing, Corros. Sci. 170 (2020).

[18] A. Harte, M. Atkinson, A. Smith, C. Drouven, S. Zaefferer, J. Quinta da Fonseca, M. Preuss, The effect of solid solution and gamma prime on the deformation modes in Ni-based superalloys, Acta Mater. 194 (2020) 257–275, https://doi.org/10.1016/j.actamat.2020.04.004.

[19] D. Texier, J. Genée, V. Velay, A.C. Moreno, D. Monceau, E. Andrieu, Size effects on the plastic behavior of polycrystalline materials: grain size, precipitation state and free-surface effects, Int. J. Plast. 188 (2025) 104284, https://doi.org/10.1016/j.ijplas.2025.104284.

[20] J. Stinville, W. Lenthe, M. Echlin, P. Callahan, D. Texier, T. Pollock, Microstructural statistics for fatigue crack initiation in polycrystalline nickel-base superalloys, Int. J. Fract. 208 (2017) 221–240, https://doi.org/10.1007/s10704-017-0241-z.

[21] J.H. Liu, N. Vanderesse, J.-C. Stinville, T.M. Pollock, P. Bocher, D. Texier, In-plane and out-of-plane deformation at the sub-grain scale in polycrystalline materials assessed by confocal microscopy, Acta Mater. 169 (2019) 260–274, https://doi.org/10.1016/j.actamat.2019.03.001, https://www.sciencedirect.com/science/article/pii/S135964541930134X.

[22] J.C. Stinville, M.A. Charpagne, A. Cervellon, S. Hemery, F. Wang, P.G. Callahan, V. Valle, T.M. Pollock, On the origins of fatigue strength in crystalline metallic materials, Science 377 (2022) 1065–1071.

[23] J. Stinville, M. Charpagne, F. Bourdin, P. Callahan, Z. Chen, M. Echlin, D. Texier, J. Cormier, P. Villechaise, T. Pollock, V. Valle, Measurement of elastic and rotation fields during irreversible deformation using Heaviside-digital image correlation, Mater. Charact. 169 (2020) 110600, https://doi.org/10.1016/j.matchar.2020.110600, https://www.sciencedirect.com/science/article/pii/S1044580320320714.

[24] D. Texier, J. Milanese, M. Jullien, J. Genée, J.-C. Passieux, D. Bardel, E. Andrieu, M. Legros, J.-C. Stinville, Strain localization in the Alloy 718 Ni-based superalloy: from room temperature to 650 °C, Acta Mater. 268 (2024) 119759, https://doi.org/10.1016/j.actamat.2024.119759.

[25] M. Charpagne, J. Hestroffer, A. Polonsky, M. Echlin, D. Texier, et al., Slip localization in Inconel 718: a three-dimensional and statistical perspective, Acta Mater. 215 (2021).

[26] R. Black, D. Anjaria, J. Genée, V. Valle, J. Stinville, Micro-strain and cyclic slip accumulation in a polycrystalline nickel-based superalloy, Acta Mater. 266 (2024).

[27] S. Ghorbanpour, S. Sahu, K. Deshmukh, E. Borisov, T. Riemslag, E. Reinton, V. Bertolo, Q. Jiang, A. Popovich, A. Shamshurin, M. Knezevic, V. Popovich, Effect of microstructure induced anisotropy on fatigue behaviour of functionally graded Inconel 718 fabricated by additive manufacturing, Mater. Charact. 179 (2021) 111350, https://doi.org/10.1016/j.matchar.2021.111350.

[28] Y. Torres, P. Trueba, J. Pavón, E. Chicardi, P. Kamm, F. García-Moreno, J. Rodríguez-Ortiz, Design, processing and characterization of titanium with radial graded porosity for bone implants, Mater. Des. 110 (2016) 179–187, https://doi.org/10.1016/j.matdes.2016.07.135.

[29] J. Wang, Z. Pan, Y. Ma, Y. Lu, C. Shen, D. Cuiuri, H. Li, Characterization of wire arc additively manufactured titanium aluminide functionally graded material: microstructure, mechanical properties and oxidation behaviour, Mater. Sci. Eng. A 734 (2018) 110–119, https://doi.org/10.1016/j.msea.2018.07.097.

[30] B.E. Carroll, R.A. Otis, J.P. Borgonia, J. ook Suh, R.P. Dillon, A.A. Shapiro, D.C. Hofmann, Z.-K. Liu, A.M. Beese, Functionally graded material of 304L stainless steel and inconel 625 fabricated by directed energy deposition: characterization and thermodynamic modeling, Acta Mater. 108 (2016) 46–54, https://doi.org/10.1016/j.actamat.2016.02.019.

[31] D. Texier, T. Richeton, H. Proudhon, A. Dziri, Q. Sirvin, M. Legros, Increase in elastic and hardness anisotropy of titanium with oxygen uptake due to high temperature oxidation: a multimodal framework using high speed nanoindentation mapping, Mater. Charact. 216 (2024) 114244, https://doi.org/10.1016/j.matchar.2024.114244.

[32] M. Legros, M. Cabié, D.S. Gianola, In situ deformation of thin films on substrates, Microsc. Res. Tech. 72 (2009) 270–283, https://doi.org/10.1002/jemt.20680.

[33] E. Paccou, B. Tanguy, M. Legros, Micropillar compression study of Fe-irradiated 304L steel, Scr. Mater. 172 (2019) 56–60, https://doi.org/10.1016/j.scriptamat.2019.07.007.

[34] X. Zhang, Y. Xiang, Combinatorial approaches for high-throughput characterization of mechanical properties, J. Materiomics 3 (2017) 209–220, https://doi.org/10.1016/j.jmat.2017.07.002.

[35] D.B. Miracle, M. Li, Z. Zhang, R. Mishra, K.M. Flores, Emerging capabilities for the high-throughput characterization of structural materials, Annu. Rev. Mater. Res. 51 (2021) 131–164, https://doi.org/10.1146/annurev-matsci-080619-022100.

[36] D.S. Gianola, N.M. della Ventura, G.H. Balbus, P. Ziemke, M.P. Echlin, M.R. Begley, Advances and opportunities in high-throughput small-scale mechanical testing, Curr. Opin. Solid State Mater. Sci. 27 (2023) 101090, https://doi.org/10.1016/j.cossms.2023.101090.

[37] C.M. Magazzeni, H.M. Gardner, I. Howe, P. Gopon, J.C. Waite, D. Rugg, D.E.J. Armstrong, A.J. Wilkinson, Nanoindentation in multi-modal map combinations: a correlative approach to local mechanical property assessment, J. Mater. Res. 36 (2021) 2235–2250, https://doi.org/10.1557/s43578-020-00035-y.

[38] E. Rossi, J.M. Wheeler, M. Sebastiani, High-speed nanoindentation mapping: a review of recent advances and applications, Curr. Opin. Solid State Mater. Sci. 27 (2023) 101107, https://doi.org/10.1016/j.cossms.2023.101107.

[39] J.M. Wheeler, B. Gan, R. Spolenak, Combinatorial investigation of the Ni–Ta system via correlated high-speed nanoindentation and EDX mapping, Small Methods 6 (2022) 2101084, https://doi.org/10.1002/smtd.202101084.

[40] M. Seehaus, S.-H. Lee, T. Stollenwerk, J.M. Wheeler, S. Korte-Kerzel, Estimation of directional single crystal elastic properties from nano-indentation by correlation with EBSD and first-principle calculations, Mater. Des. 234 (2023) 112296, https://doi.org/10.1016/j.matdes.2023.112296.

[41] A. Orozco-Caballero, C. Gutierrez, B. Gan, J.M. Molina-Aldareguia, High-throughput nanoindentation mapping of cast IN718 nickel-based superalloys: influence of the Nb concentration, J. Mater. Res. 36 (2021) 2213–2222, https://doi.org/10.1557/s43578-021-00133-5.

[42] Y. Idrissi, T. Richeton, D. Texier, S. Berbenni, J.-S. Lecomte, Robust determination of cubic elastic constants via nanoindentation and Bayesian inference, Acta Mater. 281 (2024) 120406, https://doi.org/10.1016/j.actamat.2024.120406.

[43] D.M. Dimiduk, M.D. Uchic, T.A. Parthasarathy, Size-affected single-slip behavior of pure nickel microcrystals, Acta Mater. 53 (2005) 4065–4077, https://doi.org/10.1016/j.actamat.2005.05.023.

[44] J.R. Greer, J.T.D. Hosson, Plasticity in small-sized metallic systems: intrinsic versus extrinsic size effect, Prog. Mater. Sci. 56 (2011) 654–724, https://doi.org/10.1016/j.pmatsci.2011.01.005.

[45] D. Kiener, W. Grosinger, G. Dehm, R. Pippan, A further step towards an understanding of size-dependent crystal plasticity: in situ tension experiments of miniaturized single-crystal copper samples, Acta Mater. 56 (2008) 580–592, https://doi.org/10.1016/j.actamat.2007.10.015.

[46] N. Vanderesse, M. Lagacé, F. Bridier, P. Bocher, An open source software for the measurement of deformation fields by means of digital image correlation, Microsc. Microanal. 19 (2013) 820–821, https://doi.org/10.1017/S1431927613006090.

[47] F. Di Gioacchino, J. Quinta da Fonseca, Plastic strain mapping with sub-micron resolution using digital image correlation, Exp. Mech. 53 (2013) 743–754, https://doi.org/10.1007/s11340-012-9685-2.

[48] A.D. Kammers, S. Daly, Digital image correlation under scanning electron microscopy: methodology and validation, Exp. Mech. 53 (2013) 1743–1761, https://doi.org/10.1007/s11340-013-9782-x.

[49] J. Stinville, M. Echlin, D. Texier, F. Bridier, P. Bocher, T. Pollock, Sub-grain scale digital image correlation by electron microscopy for polycrystalline materials during elastic and plastic deformation, Exp. Mech. 56 (2016) 197–216, https://doi.org/10.1007/s11340-015-0083-4.

[50] T.E.J. Edwards, F. Di Gioacchino, R. Muñoz-Moreno, W.J. Clegg, Deformation of lamellar TiAl alloys by longitudinal twinning, Scr. Mater. 118 (2016) 46–50, https://doi.org/10.1016/j.scriptamat.2016.03.004.

[51] Y. Guan, B. Chen, J. Zou, T.B. Britton, J. Jiang, F.P. Dunne, Crystal plasticity modelling and HR-DIC measurement of slip activation and strain localization in single and oligo-crystal Ni alloys under fatigue, Int. J. Plast. 88 (2017) 70–88, https://doi.org/10.1016/j.ijplas.2016.10.001.

[52] Z. Chen, S. Daly, Active slip system identification in polycrystalline metals by Digital Image Correlation (DIC), Exp. Mech. 57 (2017) 115–127, https://doi.org/10.1007/s11340-016-0217-3.

[53] F. Bourdin, J.C. Stinville, M.P. Echlin, P.G. Callahan, W.C. Lenthe, C.J. Torbet, D. Texier, F. Bridier, J. Cormier, P. Villechaise, T.M. Pollock, V. Valle, Measurements of plastic localization by Heaviside-digital image correlation, Acta Mater. 157 (2018) 307–325, https://doi.org/10.1016/j.actamat.2018.07.013.

[54] X. Xu, D. Lunt, R. Thomas, R.P. Babu, A. Harte, M. Atkinson, J.Q. da Fonseca, M. Preuss, Identification of active slip mode in a hexagonal material by correlative scanning electron microscopy, Acta Mater. 175 (2019) 376–393, https://doi.org/10.1016/j.actamat.2019.06.024.

[55] T. Vermeij, R. Peerlings, M. Geers, J. Hoefnagels, Automated identification of slip system activity fields from digital image correlation data, Acta Mater. 243 (2023) 118502, https://doi.org/10.1016/j.actamat.2022.118502.

[56] W. Yin, F. Briffod, H. Hu, T. Shiraiwa, M. Enoki, Three-dimensional configuration of crystal plasticity in stainless steel assessed by high resolution digital image correlation and confocal microscopy, Int. J. Plast. 170 (2023) 103762, https://doi.org/10.1016/j.ijplas.2023.103762.

[57] A. Rouwane, D. Texier, S. Hémery, J.-C. Passieux, Q. Sirvin, J. Genée, A. Proietti, J.-C. Stinville, Strain localization in Ti and Ti-alloys using three-dimensional topographic imaging, in: Titanium 2023, 2023, https://doi.org/10.7490/f1000research.1119929.1.

[58] P. Damas Resende, D. Texier, J. Genée, M. Jullien, H. Proudhon, J. Réthoré, D. Bardel, W. Ludwig, Slip localization and grain boundary sliding analysis at sub-voxel resolution using phase contrast tomography, Tomogr. Mater. Struct. 8 (2025) 100060, https://doi.org/10.1016/j.tmater.2025.100060.

[59] A. Dziri, K. Ammar, S. Forest, H. Proudhon, Q. Sirvin, T. Richeton, D. Texier, Effect of oxygen content on elastic properties of an oxygen-graded titanium experimental and computational frameworks, Mater. Des. (2025) 114801, https://doi.org/10.1016/j.matdes.2025.114801.

[60] D. Texier, D. Monceau, J.-C. Salabura, R. Mainguy, E. Andrieu, Micromechanical testing of ultrathin layered material specimens at elevated temperature, Mater. High Temp. 33 (2016) 325–337, https://doi.org/10.1080/09603409.2016.1182250.

[61] A. Kammers, S. Daly, Self-assembled nanoparticle surface patterning for improved digital image correlation in a scanning electron microscope, Exp. Mech. 53 (2013) 1333–1341, https://doi.org/10.1007/s11340-013-9734-5.

[62] C. Montgomery, B. Koohbor, N. Sottos, A robust patterning technique for electron microscopy-based digital image correlation at sub-micron resolutions, Exp. Mech. 59 (2019) 1063–1073, https://doi.org/10.1007/s11340-019-00487-2.

[63] A.W. Mello, T.A. Book, A. Nicolas, S.E. Otto, C.J. Gilpin, M.D. Sangid, Distortion correction protocol for digital image correlation after scanning electron microscopy: emphasis on long duration and ex-situ experiments, Exp. Mech. (2017), https://doi.org/10.1007/s11340-017-0303-1.

[64] V. Valle, S. Hedan, P. Cosenza, A.L. Fauchille, M. Berdjane, Digital image correlation development for the study of materials including multiple crossing cracks, Exp. Mech. 55 (2015) 379–391, https://doi.org/10.1007/s11340-014-9948-1.

[65] J.C. Stinville, J.M. Hestroffer, M.A. Charpagne, A.T. Polonsky, M.P. Echlin, C.J. Torbet, V. Valle, A. Loghin, O. Klaas, M.P. Miller, K.E. Nygren, I.J. Beyerlein, T.M. Pollock, Multi-modal dataset of a polycrystalline metallic material: 3D microstructure and deformation fields, https://doi.org/10.5061/DRYAD.83BK3J9SJ, 2022, https://datadryad.org/dataset/doi:10.5061/dryad.83bk3j9sj.

[66] D. Anjaria, J.-C. Stinville, In-situ tensile test scanning electron microscopy dataset for solutionized Inconel 718, 10.5061/DRYAD.98SF7M0TT, 2025, https://datadryad.org/dataset/doi:10.5061/dryad.98sf7m0tt.

[67] F. Pöhl, Pop-in behavior and elastic-to-plastic transition of polycrystalline pure iron during sharp nanoindentation, Sci. Rep. 9 (2019) 15350, https://doi.org/10.1038/s41598-019-51644-5.

[68] P. Villechaise, J. Cormier, T. Billot, J. Mendez, Mechanical behaviour and damage processes of UDIMET 720Li: influence of localized plasticity at grain boundaries, Superalloys 2012 (2012) 15–24.

[69] X. Zhao, J. Wu, Y. Chiu, I. Jones, R. Gu, A. Ngan, Critical dimension for the dislocation structure in deformed copper micropillars, Scr. Mater. 163 (2019) 137–141, https://doi.org/10.1016/j.scriptamat.2019.01.020.

[70] P. Ispánovity, D. Ugi, G. Péterffy, et al., Dislocation avalanches are like earthquakes on the micron scale, Nat. Commun. 13 (2022), https://doi.org/10.1038/s41467-022-29044-7.

[71] R. Azihari, Approche micromécanique et modélisation de la rupture intergranulaire: application à la corrosion sous contrainte assistée par l'irradiation, Ph.D. thesis, Université de Toulouse, 2023.

[72] K. Goto, I. Watanabe, T. Ohmura, Inverse estimation approach for elastoplastic properties using the load-displacement curve and pile-up topography of a single Berkovich indentation, Mater. Des. 194 (2020) 108925, https://doi.org/10.1016/j.matdes.2020.108925.

[73] K. Goto, A. Ikeda, T. Osada, I. Watanabe, K. Kawagishi, T. Ohmura, High-throughput evaluation of stress–strain relationships in ni–co–cr ternary systems via indentation testing of diffusion couples, J. Alloys Compd. 910 (2022) 164868, https://doi.org/10.1016/j.jallcom.2022.164868.

[74] Julia Hütsch, Erica T. Lilleodden, The influence of focused-ion beam preparation technique on microcompression investigations: lathe vs. annular milling, Scr. Mater. 77 (2014) 49–51, https://doi.org/10.1016/j.scriptamat.2014.01.016.

[75] J. Zimmermann, S. Van Petegem, H. Bei, D. Grolimund, E. George, H. Van Swygenhoven, Effects of focused ion beam milling and pre-straining on the microstructure of directionally solidified molybdenum pillars: a laue diffraction analysis, Scr. Mater. 62 (2010) 746–749, https://doi.org/10.1016/j.scriptamat.2010.02.013.

[76] S. Shim, H. Bei, M. Miller, G. Pharr, E. George, Effects of focused ion beam milling on the compressive behavior of directionally solidified micropillars and the nanoindentation response of an electropolished surface, Acta Mater. 57 (2009) 503–510, https://doi.org/10.1016/j.actamat.2008.09.033.